Available online at www.sciencedirect.com
ScienceDirect
Precambrian Research 162 (2008) 354–384
Precambrian Research
www.elsevier.com/locate/precamres

Proterozoic deformation in the northwest of the Archean Yilgarn Craton, Western Australia

Catherine V. Spaggiari [a,*], Jo-Anne Wartho [b,1], Simon A. Wilde [b]

[a] *Geological Survey of Western Australia, Department of Industry and Resources, 100 Plain Street, East Perth, Western Australia 6004, Australia*
[b] *Department of Applied Geology, Curtin University, GPO Box U1987, Perth, Western Australia 6845, Australia*

Received 31 January 2007; received in revised form 19 September 2007; accepted 16 October 2007

Abstract

The Narryer Terrane within the northwestern Yilgarn Craton contains the oldest crust in Australia. The Jack Hills greenstone belt is located within the southern part of the Narryer Terrane, and structures cutting it and surrounding rocks have been dated using the $^{40}Ar/^{39}Ar$ technique. The results show that east-trending, dextral, transpressive shearing was related to the 1830–1780 Ma Capricorn Orogeny, followed by further deformation and/or cooling between c. 1760 and 1740 Ma. These results confirm that major deformation has affected the northwestern part of the Yilgarn Craton in an intracratonic setting during the Proterozoic. Proterozoic structures have been interpreted to extend south beyond the Narryer Terrane into the northern part of the Youanmi Terrane (Murchison Domain), and include the Yalgar Fault, previously interpreted as the boundary between the Narryer and Youanmi Terranes. Terrane amalgamation pre-dated the emplacement of c. 2660 Ma granites in both terranes, and the current expression of the Yalgar Fault must represent a younger, reworked, post-amalgamation structure, possibly controlled by the tectonic boundary. However, new aeromagnetic and gravity imagery does not show the eastern part of the Yalgar Fault as a major structure. Its signature is more akin to a series of east- to east-northeast trending faults that are interpreted to be Proterozoic in age. This suggests that this part of the Yalgar Fault may not be a terrane boundary, and is possibly no older than Proterozoic. The $^{40}Ar/^{39}Ar$ dating also shows a younger, less intense deformation and/or cooling event at c. 1172 Ma.

Keywords: Jack Hills; Narryer Terrane; Yilgarn Craton; $^{40}Ar/^{39}Ar$ data; Capricorn Orogeny; Yalgar Fault

1. Introduction

Understanding the nature and timing of deformation events within the Yilgarn Craton generally requires dating of unconformities or cross-cutting intrusions. However, poor exposure and heterogeneous strain relationships in the craton have often inhibited correlation of deformation sequences. Major deformation throughout the Narryer Terrane and Murchison Domain of the Youanmi Terrane (Fig. 1) has mostly been interpreted to be Neoarchean (Myers, 1990a), but this has been poorly constrained because it is difficult to date directly, and because of the heterogeneous deformation relationships within the Neoarchean granitic rocks (e.g., Schiøtte and Campbell, 1996; Spaggiari, 2006). Although Proterozoic overprinting of Archean structures in the northwestern part of the Yilgarn Craton has previously been interpreted (e.g., Williams et al., 1983a; Williams, 1986; Myers, 1997) no data from direct dating of the structures or fabrics has been published. In this study we have attempted to determine the age of specific deformation and cooling events in the northwestern part of the craton using the $^{40}Ar/^{39}Ar$ technique.

The Narryer Terrane makes up most of the northwestern Yilgarn Craton, and is bound by the Youanmi Terrane to the south (Fig. 1). The Youanmi Terrane comprises the Murchison and Southern Cross Domains (Cassidy et al., 2006), which are made up almost entirely of Archean granitic rocks, greenstones, and mafic-ultramafic intrusions. The Narryer Terrane is distinct because it contains older, predominantly granitic gneisses that range in age from c. 3730 to 3300 Ma (e.g. Kinny et al., 1990; Nutman et al., 1991; Kinny and Nutman, 1996; Pidgeon and Wilde, 1998), but it is not clear whether the Narryer Terrane is truly exotic to the Youanmi Terrane,

* Corresponding author. Tel.: +61 8 9222 3491; fax: +61 8 9222 3633.
E-mail address: Catherine.Spaggiari@doir.wa.gov.au (C.V. Spaggiari).
[1] Current address: School of Earth and Space Exploration, Arizona State University, P.O. Box 871404, Tempe, AZ 85287-1404, USA.

0301-9268/$ – see front matter © 2007 Published by Elsevier B.V.
doi:10.1016/j.precamres.2007.10.004

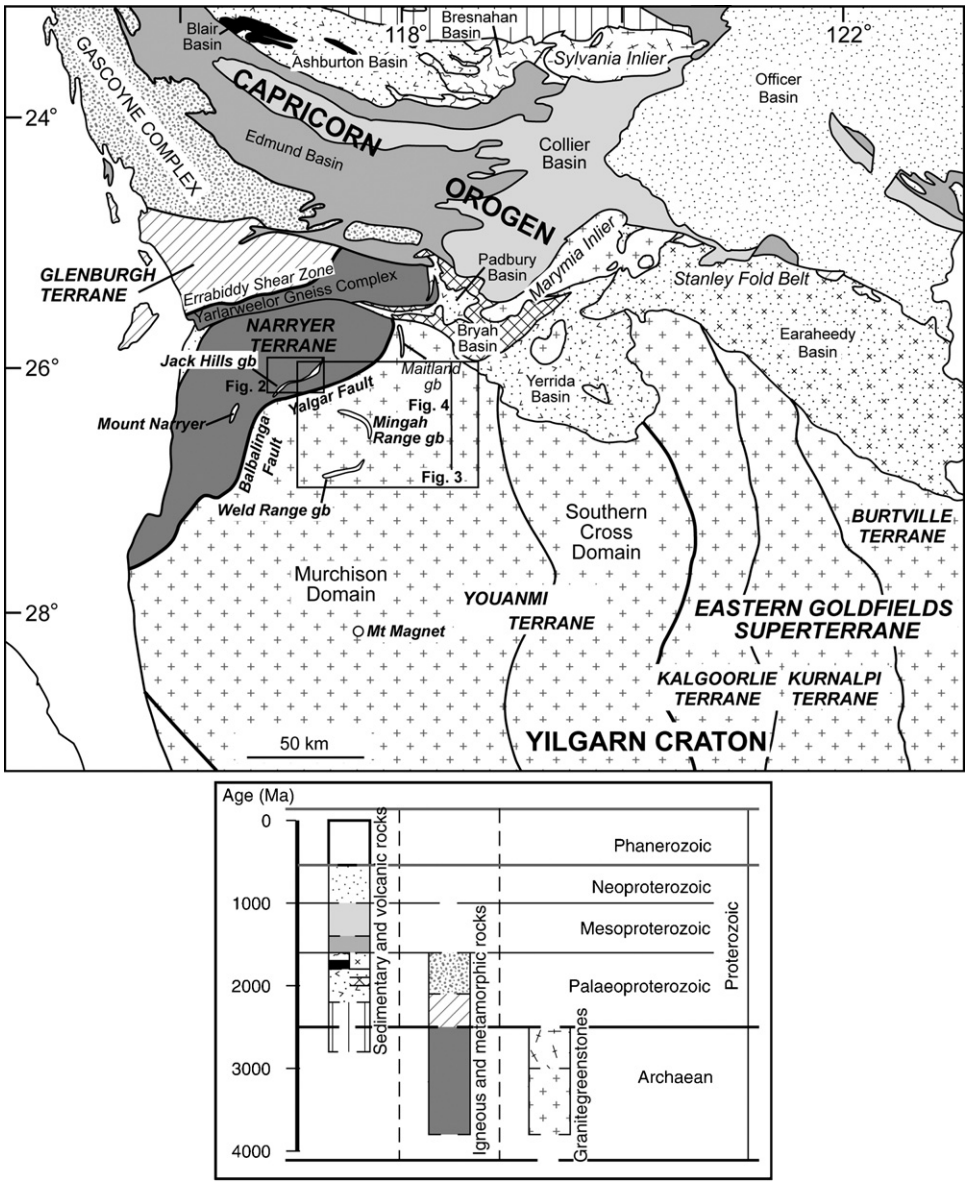

Fig. 1. Map of the Yilgarn Craton and Capricorn Orogen showing tectonic subdivisions, and location of the Jack Hills greenstone belt (modified from Cawood and Tyler, 2004; Cassidy et al., 2006). gb = greenstone belt.

or whether the Narryer Terrane is an exposed part of the Youanmi Terrane basement. Detrital zircons from quartzites in the Southern Cross Domain (Fig. 1) range in age from c. 4350 to 3130 Ma, and are older than any other rocks in the Youanmi Terrane, but are similar to ages of granitic gneisses and detrital zircons in the Narryer Terrane (Wyche et al., 2004). This could indicate that a common, c. 3.1 Ga-or-older basement was reworked and incorporated into the Younami Terrane, but was preserved in the Narryer Terrane (Wyche et al., 2004). The Youanmi–Narryer terrane boundary is presently defined by the Yalgar and Balbalinga Faults (Myers, 1990a, 1993, 1997; Myers and Hocking, 1998). These faults have been interpreted as a zone of suturing between the two terranes, formed in the late Archean between c. 2.68 and 2.65 Ga, with the Yalgar Fault being reactivated in the early Proterozoic (Myers, 1990b, 1995, 1997).

The northern margin of the Narryer Terrane, including the Errabiddy Shear Zone and Yarlarweelor Gneiss Complex (Fig. 1), was deformed in the Paleoproterozoic during both the 2005–1960 Ma Glenburgh Orogeny and the 1830–1780 Ma Capricorn Orogeny (Occhipinti et al., 2004; Sheppard et al., 2003). The Errabiddy Shear Zone initially formed during accretion of an Andean-type magmatic arc and microcontinent (the Glenburgh Terrane) to the northern margin of the craton, resulting in interleaving of the craton margin with Paleoproterozoic rocks, development of subhorizontal or gently dipping faults, folds, and foliations, and medium to high grade metamorphism (Sheppard et al., 2004; Occhipinti et al., 2004). These structures were overprinted during the Capricorn Orogeny by tight, upright folds and dextral transpressional shear zones predominantly under greenschist facies conditions (Occhipinti and Reddy, 2004).

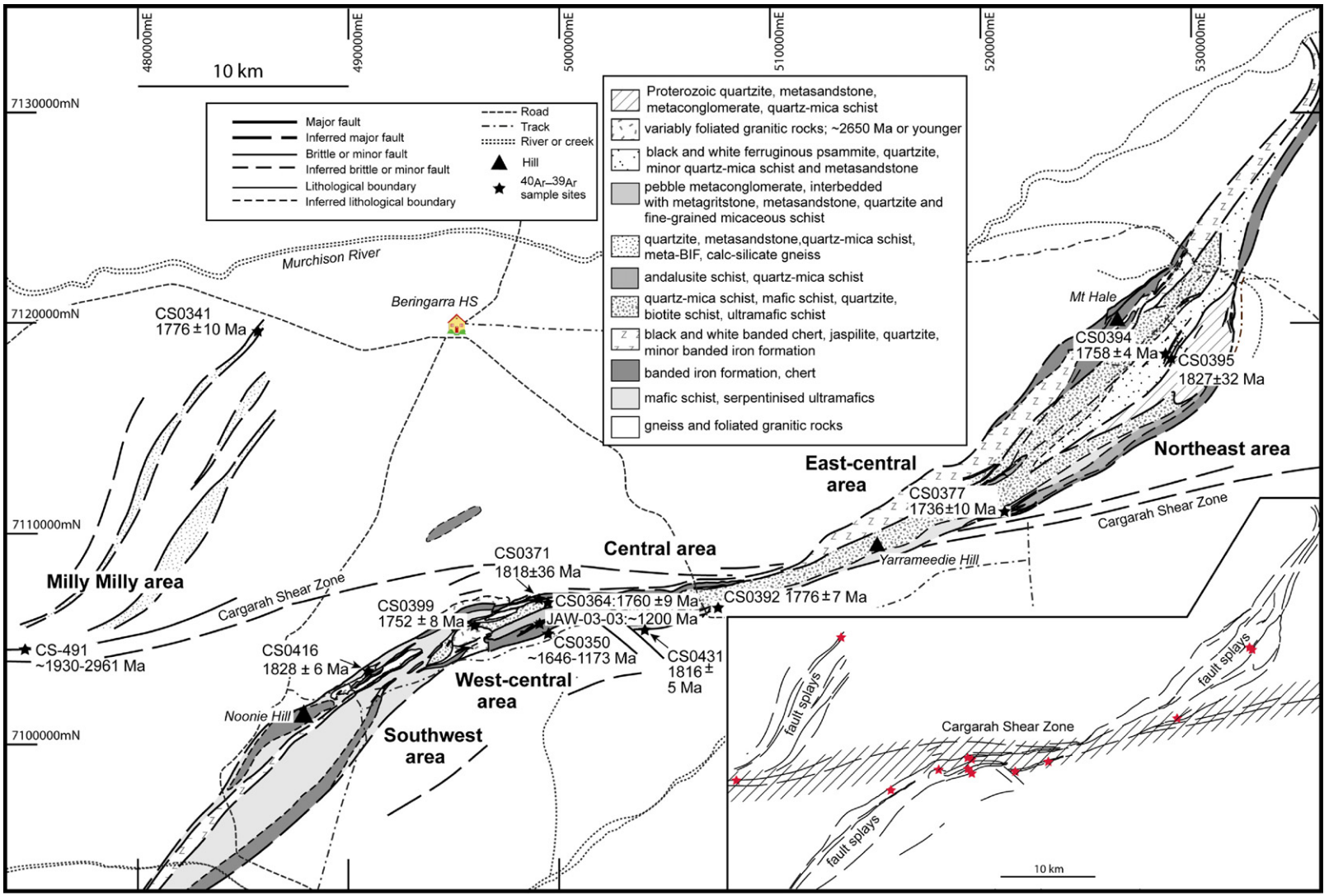

Fig. 2. Simplified geological map of the Jack Hills greenstone belt showing sample locations and their average or weighted mean $^{40}Ar/^{39}Ar$ ages (modified from Spaggiari, 2007a). The inset shows the structural outline of the belt and the dominant area affected by the Cargarah Shear Zone, with the sample locations overlain.

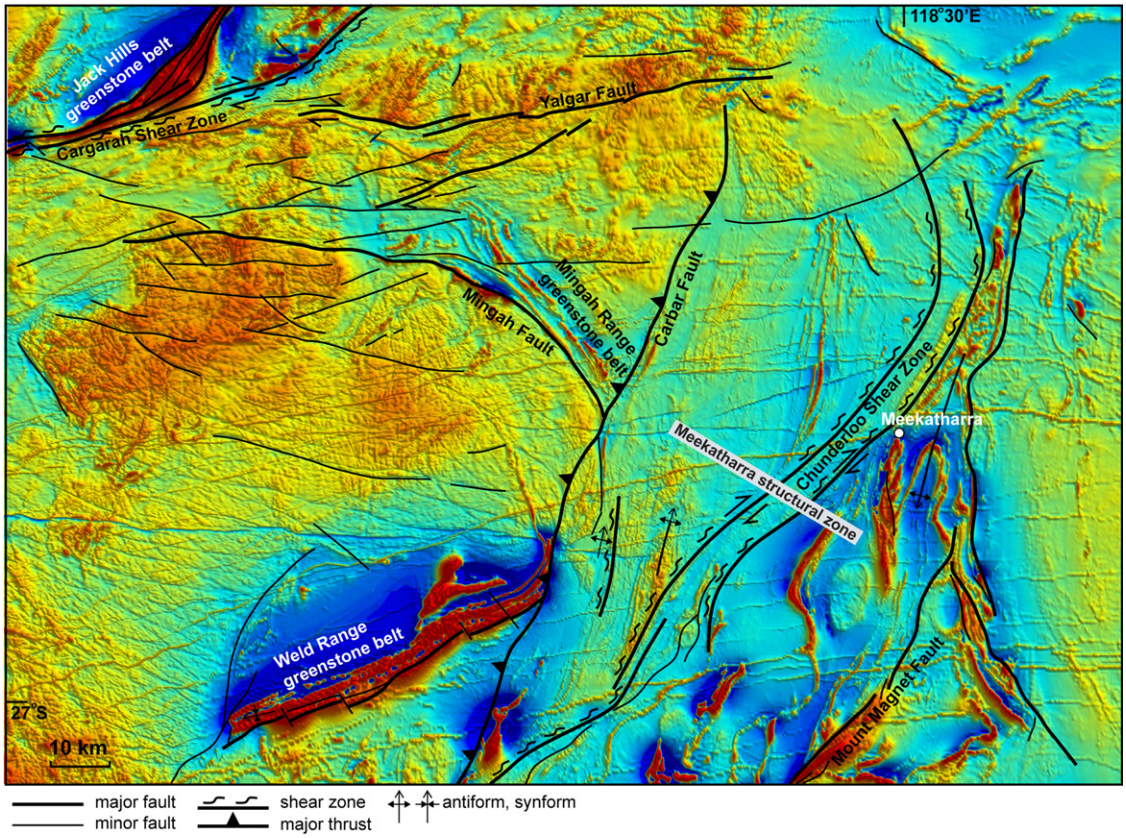

Fig. 3. Simplified structural interpretation of the southeastern Narryer Terrane and northern Murchison Domain, showing the location of the Yalgar Fault, Carbar Fault, and Meekatharra structural zone (after Spaggiari, 2006; based on Geological Survey of Western Australia, 2006). Only the eastern half of the Jack Hills greenstone belt and Cargarah Shear Zone are shown because this is the limit of 400 m or less line spacing aeromagnetic data.

In this paper, we present the results of $^{40}Ar/^{39}Ar$ analyses from thirteen samples collected in and around the Jack Hills greenstone belt in the southeastern Narryer Terrane (Fig. 2). The results show that Paleoproterozoic deformation and cooling events are mostly related to the Capricorn Orogeny (*cf.* Williams et al., 1983a; Williams, 1986; Myers, 1995, 1997). Related structures are also interpreted to extend into the northwestern Murchison Domain, based largely on geophysical images. Our data also indicates post-Capricorn Orogeny (<1780 Ma) reworking in the Jack Hills area. The Jack Hills area was chosen for this $^{40}Ar/^{39}Ar$ study because it was also the focus of a detailed structural and lithological study (Spaggiari, 2007a,b; Spaggiari et al., 2007), which allowed specific deformation fabrics to be targeted. The $^{40}Ar/^{39}Ar$ age data are a combination of *in situ* ultra-violet (UV) laser step-heating analyses of white mica and biotite, and infra-red (IR) step-heating analyses of white mica, biotite, and hornblende mineral separates and individual grains. Complexities in the dating of strongly and multiply deformed rocks using the $^{40}Ar/^{39}Ar$ method, such as partial resetting of the ages, are well documented (e.g., Reddy and Potts, 1999; Kramar et al., 2001). The different $^{40}Ar/^{39}Ar$ laser dating techniques were chosen to help see through these complexities in order to constrain the absolute deformation and cooling ages of the rocks.

2. Geological setting

The Narryer Terrane is dominated by 3730–3300 Ma granitic rocks and granitic gneisses that are locally interleaved with slivers of metamorphosed supracrustal rocks, including banded iron formation (BIF), calc-silicates, mafic and ultramafic rocks, and metasedimentary rocks predominantly metamorphosed under granulite facies conditions (Williams and Myers, 1987; Myers, 1988; Kinny et al., 1988, 1990). The gneisses contain evidence of three phases of folding, and, although not well-constrained, the deformation that produced the regional tectonic fabric is interpreted to have occurred at granulite facies conditions, but largely retrogressed to amphibolite facies conditions, between c. 2750 and 2600 Ma, during and/or prior to intrusion of Neoarchean granites (Myers, 1990a; Occhipinti et al., 2001). The most extensive occurrences of metasedimentary rocks are in the vicinity of Mount Narryer and Jack Hills (Fig. 1). Both localities are well-known for their ≥4.0 Ga detrital zircon populations (e.g., Froude et al., 1983; Compston and Pidgeon, 1986; Wilde et al., 2001). In the vicinity of Mount Narryer, amphibolite to granulite facies metasedimentary rocks are dominated by quartzites (Williams and Myers, 1987). Together with the granitic gneisses, the metasedimentary rocks are folded isoclinally into east-trending folds that are refolded by north-trending folds. Both sets of

folds are cut by mylonitic shear zones (Williams and Myers, 1987). The Mount Narryer metasedimentary rocks were metamorphosed at higher temperatures than the rocks of the Jack Hills greenstone belt, which contain assemblages indicative of upper greenschist to amphibolite facies conditions (Elias, 1982; Wilde and Pidgeon, 1990).

The Murchison Domain of the Youanmi Terrane is dominated by greenstones and granitic rocks that were deposited or emplaced between c. 3000–2600 Ma. Geochronological data for the greenstones are limited but the oldest felsic volcanic rocks formed at c. 3000 and 2950 Ma (Pidgeon and Wilde, 1990; Pidgeon et al., 1994; Wang et al., 1998) and the majority of felsic volcanic rocks formed between c. 2800–2700 Ma (Schiøtte and Campbell, 1996; Pidgeon and Hallberg, 2000; see Spaggiari, 2006 for a review). Along the northern margin of the western part of the Weld Range greenstone belt (Figs. 1 and 3), lithic sandstone of probable volcanic provenance is interbedded with BIF and contains a unimodal detrital zircon population of 2970 ± 4 Ma (U–Pb Sensitive High-Resolution Ion Microprobe (SHRIMP), 1σ error, sample GSWA 184112, Bodorkos and Wingate, in preparation). This provides a maximum depositional age for the BIF. Given the unimodal population (n = 46), the zircons may have been associated with a magmatic event that produced the felsic volcanic rocks that flank the interbedded BIF on the northern margin of the Weld Range. This suggests that the BIF was probably deposited close to this time, i.e., syn- or post-felsic volcanism. Most of the granitic rocks of the Murchison Domain formed between c. 2750–2610 Ma, with a major, craton-wide geochemical change at c. 2655 Ma from dominantly high-Ca to dominantly low-Ca granitic magmatism (Cassidy et al., 2002).

The major regional structures of the northern Murchison Domain are northeast-trending and north- to northwest-trending folds, faults, and shear zones. Early east-trending folds (D_2 of Watkins and Hickman, 1990) are preserved locally, but appear to be confined to the west of a major west-dipping thrust, the Carbar Fault, that separates the Weld Range and Mingah Range greenstone belts from the Meekatharra structural zone (Fig. 3; Spaggiari, 2006). The Meekatharra structural zone is an approximately 50–60 km wide, northeast-trending, shear-dominated zone incorporating the Meekatharra–Wydgee greenstone belt, and the majority of historic gold deposits in the Murchison Domain (Spaggiari, 2006). Nd model ages of granitic rocks within the zone indicate slightly younger crustal sources of c. 3.1–2.9 Ga, compared to c. 3.3–3.1 Ga from the surrounding granitic rocks of the Murchison Domain (Cassidy et al., 2002). This suggests that the Meekatharra structural zone may have initially developed as a small rift basin, possibly from c. 2.75 Ga. The timing of deformation in the Murchison Domain is poorly constrained. Attempts to date apparently undeformed granites to use as post-deformation markers have been shown to be flawed due to the complexities of strain partitioning, i.e. the undeformed granites are often competent remnants that have escaped deformation fabric formation (Schiøtte and Campbell, 1996). The best estimate for the timing of deformation, at least in the Mt. Magnet area (Fig. 1), comes from the formation of decompression melt veins due to gneissic monzogranite emplacement at c. 2660 Ma, which was synchronous with deformation and formation of the gneissic fabric (Schiøtte and Campbell, 1996). The monzogranite itself is interpreted to have crystallised at c. 2675 Ma (Schiøtte and Campbell, 1996).

Proterozoic deformation and cooling of the Narryer Terrane and part of the Murchison Domain is indicated by Rb–Sr biotite ages (Libby et al., 1999) and K–Ar and $^{40}Ar/^{39}Ar$ biotite and hornblende ages from the Mount Narryer area (Kinny et al., 1990). Libby et al. (1999) dated numerous samples from the southern Gascoyne Complex and northwestern and western Yilgarn Craton and identified four areas with different age groups. The data for one of these areas, the Narryer Terrane and part of the Murchison Domain, shows a large scatter of Rb–Sr biotite ages ranging from 1833 to 1375 Ma, with an average age of c. 1650 Ma that Libby et al. (1999) interpreted as due to resetting of the Rb–Sr systematics, which was attributed to cooling and uplift after south-directed thrusting related to the Capricorn Orogeny. Older Rb–Sr biotite ages of 2203 and 2069 Ma were preserved in the Mount Narryer area. One sample of granodioritic gneiss adjacent to the northern margin of the Jack Hills greenstone belt gave an age of 1375 Ma, and ages between 1400 and 1350 Ma in the Narryer Terrane have been interpreted to represent localised shearing (Libby et al., 1999). Note that no errors were quoted on the ages reported by Libby et al. (1999).

Kinny et al. (1990) used K–Ar to date biotite from an amphibolite from the Mount Narryer area that gave an age of 1789 ± 34 Ma (1σ). Hornblende from the same sample gave an apparent, maximum $^{40}Ar/^{39}Ar$ age of 2780 Ma. One other hornblende sample, a meta-anorthosite from the Manfred Complex, gave $^{40}Ar/^{39}Ar$ ages between 2720 and 2670 Ma. Biotite from a pelite yielded a K–Ar age of 2022 ± 44 Ma (1σ), and Meeberrie gneiss biotites gave K–Ar ages of 1887 ± 43 Ma (1σ) and 1778 ± 32 Ma (1σ). Most samples gave apparent ages of c. 2700 Ma, which Kinny et al. (1990) interpreted as cooling ages for the Mount Narryer area, with resetting at c. 2000 Ma, or partial radiogenic $^{40}Ar(^{40}Ar^*)$ loss during retrogression at c. 1600 Ma. In summary, although these ages do not precisely date any deformation and/or cooling event, they do indicate a disturbance of the Rb–Sr and K–Ar isotopic systems during the Proterozoic.

2.1. Jack Hills greenstone belt

The Jack Hills greenstone belt is situated along the southeastern margin of the Narryer Terrane and is surrounded by mostly early Archean granitic gneisses (Fig. 1). The term "greenstone belt" is generally applied to belts of rocks in the Yilgarn Craton that typically include BIF, mafic and ultramafic rocks, volcanic rocks, and metasedimentary rocks, and is therefore relevant to the Jack Hills. The belt includes a significant component of metasedimentary rocks, at least some of which are Proterozoic in age (Cavosie et al., 2004; Dunn et al., 2005; Spaggiari et al., 2007), and because of this has often been termed a supracrustal belt or metasedimentary belt. However, it does contain a significant proportion of BIF, currently being mined for iron ore, as well as mafic and ultramafic rocks, and possible metavol-

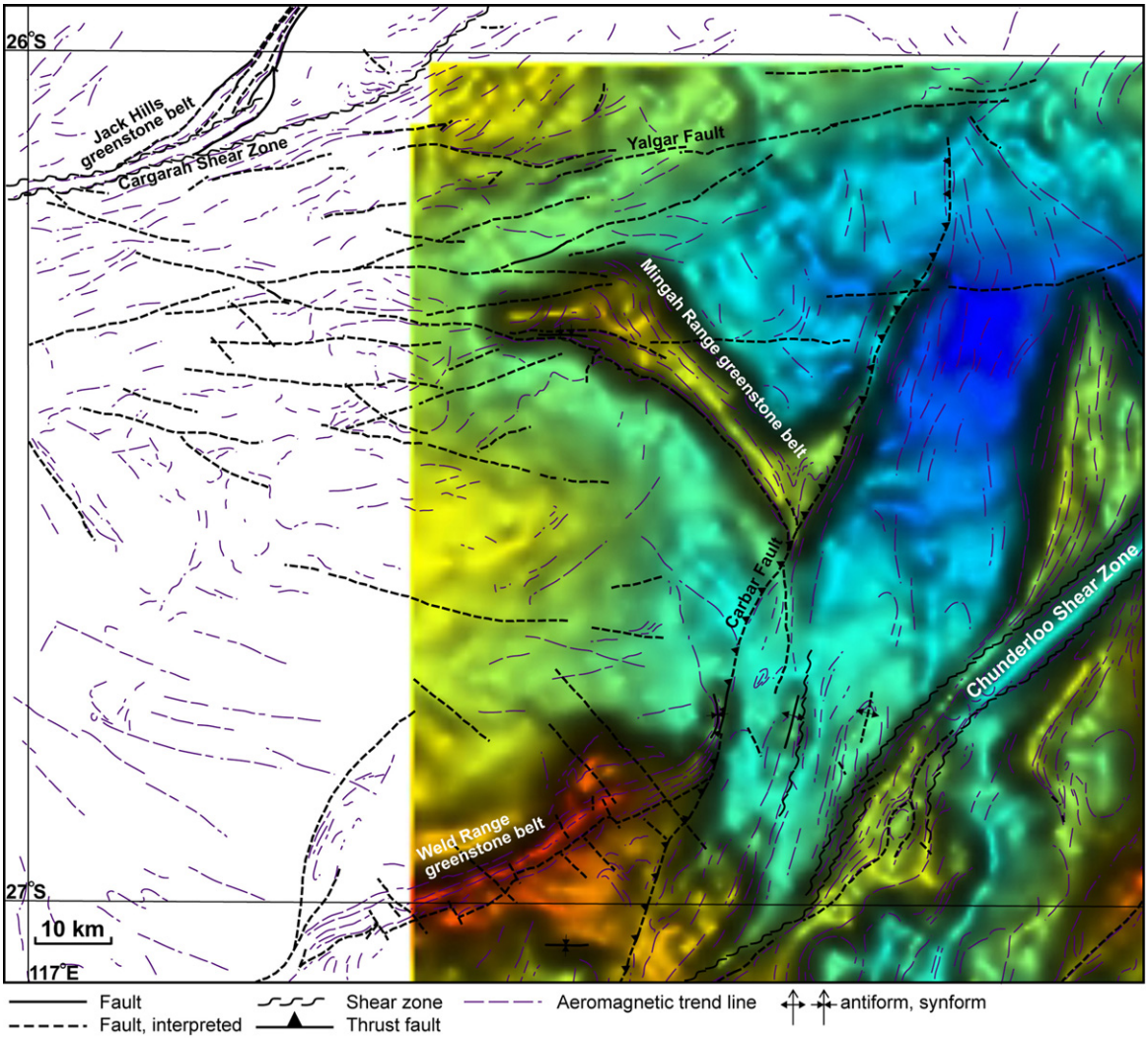

Fig. 4. Bouger gravity image of the Murchison 2007 government dataset flown using a grid interval of 2.5 km, overlain with the structural interpretation based on aeromagnetic data and Geological Survey of Western Australia mapping (Geological Survey of Western Australia, 2006). Note that the western edge of the gravity image is the limit of the data.

canic rocks (Elias, 1982; Wilde and Pidgeon, 1990; Spaggiari, 2007a). It is therefore made up of at least two components; an older "greenstone" component, and a younger metasedimentary component. Structural, lithological, and geochronological data from the belt show that it has undergone a long and complex depositional and structural evolution over a period of time ranging from c. 3000–1075 Ma (Spaggiari, 2007a,b; Spaggiari et al., 2007).

The Jack Hills greenstone belt consists of upper greenschist to amphibolite facies BIF, chert, quartzite, pelitic and semipelitic schists, and mafic and ultramafic rocks, all of which have been intruded by Neoarchean granitic rocks that yield SHRIMP U–Pb zircon ages of 2654 ± 7 Ma and 2643 ± 7 Ma (1σ) (Elias, 1982; Wilde and Pidgeon, 1990; Pidgeon and Wilde, 1998; Spaggiari et al., 2007). Structurally interleaved with these units are mature clastic rocks and a sequence of Proterozoic metasedimentary rocks. The mature clastic rocks have been the focus of much research on early Earth processes because they host detrital zircons that are $\geq$4.0 Ga (e.g., Mojzsis et al., 2001; Peck et al., 2001; Valley et al., 2002; Cavosie et al., 2005; Harrison et al., 2005; Nemchin et al., 2006).

Prior to, or synchronous with, the intrusion of the Neoarchean granitic rocks, deformation included recumbent and chevron folding that was probably associated with thrust faulting (Spaggiari, 2007b). However, the dominant structural feature of the Jack Hills greenstone belt is a major, east-trending shear zone (the Cargarah Shear Zone) that cuts the belt and has produced the present-day sigmoidal geometry (Figs. 2 and 3; Spaggiari, 2007a,b). The shear zone is defined by an ~3 to 4 km wide zone of locally mylonitic rocks that commonly contain S-C fabrics. These are interpreted to be part of a network of linked shears that together form the main shear zone. The geometry, kinematic indicators, and shear-related structures indicate that the shearing was transpressional with a dextral motion (Williams, 1986; Spaggiari, 2007b). The northeastern and southwestern parts of the Jack Hills greenstone belt are interpreted to lie within fault splays off this major shear zone (Fig. 2; Spaggiari, 2007b). The shearing clearly post-dates intrusion of the Neoarchean granitic

Table 1
Summary of samples dated by the $^{40}Ar/^{39}Ar$ technique

Sample	Location	Rock type	Petrography	^{40}Ar-^{39}Ar technique and mineral dated
CS-491 (GSWA 184303)	Milly Milly area, western Cargarah Shear Zone; within 100 m of MGA 474180mE, 7103939mN	Metadolerite sliver within orthogneiss	Hornblende, plagioclase, biotite, Fe-oxide, minor chlorite and quartz (Fig. 6a). Relict interlocking texture of ~1 mm plag laths and hornblende amphibole overgrowing pyroxene	IR-laser; hornblende separate
CS0416 (GSWA 184301)	Southwestern area; 30 m north of MGA 491092mE, 7103606mN	Muscovite granite	Quartz and twinned feldspar with interlocking texture, interstitial muscovite (Fig. 6b); muscovite grains c. 100 μm to 1 cm; foliation defined by zones of recrystallised feldspar and quartz, and aligned white mica	IR-laser; white mica separate
CS0431 (GSWA 184302)	Southern margin of central area; contact with mafic and ultramafic schist; MGA 503737mE, 7105724mN	Sheared granite	Quartz, K-feldspar, biotite; biotite laths average c. 500 μm, minor chlorite; strong foliation (Fig. 6c)	IR-laser; biotite separate
CS0395 (GSWA 184306)	Adjacent to major fault in northeastern area; MGA 529034mE, 7118818mN	Quartz-mica mylonitic schist interbedded with quartzite	Quartz, white mica, andalusite; quartz-rich, elongate 1–2 cm aggregates of recrystallised quartz wrapped by micaceous foliation; small andalusite porphyroblasts wrapped by the foliation (Fig. 6f)	UV-laser; white mica in situ (thick section)
CS0394	Northeastern area; MGA 529000mE, 7118920mN	Quartz-mica mylonitic schist	Quartz, white mica, andalusite, minor chlorite; strong mylonitic foliation defined by quartz, white mica, chlorite; micaceous and chloritic pressure shadows off andalusite porphyroblasts (Fig. 6d)	UV-laser; white mica in situ (Fig. 6e; thick section)
CS0377	East-central area; MGA 521373mE, 7111170mN	Quartz-mica mylonitic schist (Fig. 6g)	Quartz, white mica, andalusite, chlorite; white mica comprises both muscovite and sericite; small poikiloblastic andalusite porphyroblasts, partly sericitised; micaceous pressure shadows off andalusite and quartz porphyroblasts	UV-laser; white mica in situ (thick section)
CS0392	Central area; MGA 507165mE, 7106433mN	Sheared pegmatite in orthogneiss	Not done	UV-laser; white mica separate
CS0371	Semi-brittle fault zone near the northern margin of the west-central area (Fig. 6h); MGA 498345mE, 7106653mN	Deformed pegmatite	Not done	UV-laser; white mica separate
CS0364	Northern west-central area; MGA 498818mE, 7106426mN	Quartz-biotite schist	Quartz, biotite, white mica, minor chlorite, Fe-oxide; strong biotite and quartz foliation, pressure shadows off Fe-oxide; relict detrital tourmaline (Fig. 6i)	UV-laser; biotite and white mica in situ (thick section)
JAW-03-03	Phyllite around a boudinaged quartz vein within a semi-brittle fault zone; southern west-central area (Fig. 6j); MGA 499135mE, 71055844mN	Quartz-mica schist	Not done	UV-laser; white mica separate
CS0350	Southern margin, west-central area; MGA 499471mE, 7105311mN	Granitic gneiss (Fig. 6k)	Quartz, K-feldspar, biotite, white mica, garnet; porphyroclasts of K-feldspar (Fig. 6l)	UV-laser; white mica in situ (thick section)
CS0399	Northern margin of monzogranitic intrusion (the Blob), west-central area; MGA 495500mE, 7105568mN	Quartz-mica schist	Quartz, white mica, minor biotite, Fe-oxide; strong foliation mostly defined by quartz and white mica	UV-laser; white mica separate
CS0341	Northern Milly Milly area; MGA 485929mE, 7119422mN	Quartz-mica schist	Quartz, muscovite, sericite, minor chlorite; muscovite partly overgrown by sericite (Fig. 6m)	UV-laser; white mica in situ (thick section)

All map coordinates are given according to the WGS84 datum

rocks. The main foliation associated with the formation of the Cargarah Shear Zone is overprinted by semi-brittle and brittle structures, such as faults and kink folds, and the main shears show evidence of reactivation, with ductile shears overprinted by semi-brittle to brittle fault structures (Spaggiari, 2007a,b). The belt is dominated by a strong, steeply dipping foliation that mostly strikes parallel to the trend of the belt. The foliation has largely been coaxially overprinted during deformation related to both folding and shearing. Thus, linking foliation chronology across the belt is difficult, as earlier foliations are commonly obliterated. However, the nature of the foliations (e.g., shear bands, S–C foliations, axial planar foliations) can be characterised locally. This has permitted selective sampling for $^{40}Ar/^{39}Ar$ dating purposes. Undeformed, cross-cutting mafic dykes that are interpreted to be part of the 1075 Ma Warakurna large igneous province (Wingate et al., 2005; Spaggiari, 2007a) indicate that major deformation had ceased by that time.

2.2. Regional structural interpretation from geophysical images

Recently acquired aeromagnetic images (Geological Survey of Western Australia and Geoscience Australia government datasets) of the southeastern Narryer Terrane and northern Murchison Domain show a system of east- to east-northeast-trending faults parallel to, and south of, the Cargarah Shear Zone, and extending into the northern part of the Murchison Domain (Fig. 3). These faults truncate north to northeast-trending faults in the Meekatharra structural zone, but are cut by northwest-trending faults in the vicinity of the Jack Hills greenstone belt. Some have dextral sigmoidal geometries, similar to the Cargarah Shear Zone, which curves to the northeast, east of the Jack Hills greenstone belt.

The east- to east-northeast-trending faults truncate the northern end of the Mingah Range greenstone belt (Figs. 3 and 4), where they are steeply north-dipping and predominantly cut through granitic rocks. In outcrop they are locally mylonitic and have moderately to steeply, northeast-plunging mineral lineations that include white mica. Local, dextral S–C foliations suggest oblique normal displacement, with the north side down. The faults are commonly subparallel to large quartz veins. In contrast, the majority of rocks in the Mingah Range greenstone belt have a northwest-trending, steeply northeast or southwest-dipping foliation of variable intensity that is axial planar to both local, small-scale F_1 and F_2 tight folds (Spaggiari, 2006). The F_2 folds also fold a strong

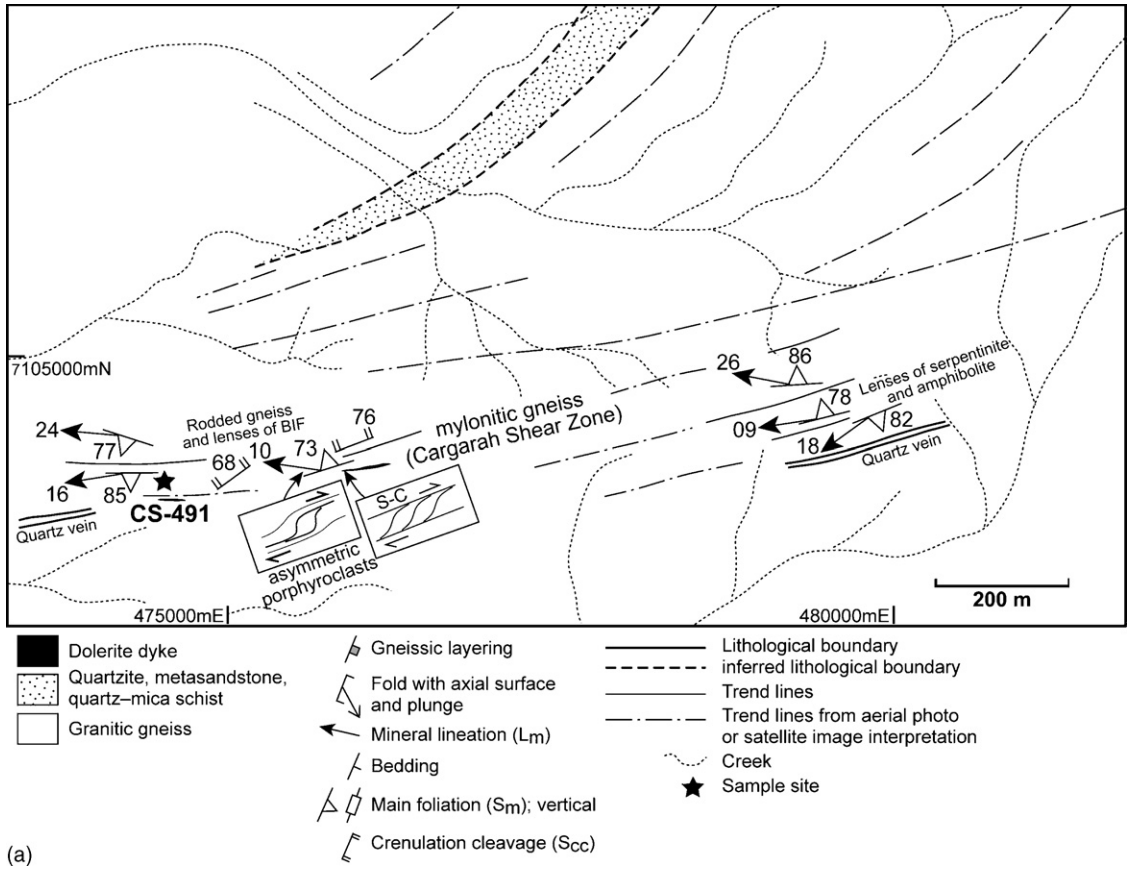

Fig. 5. Simplified geological maps showing $^{40}Ar/^{39}Ar$ sample locations (modified from Spaggiari, 2007a,b; Spaggiari et al., 2007). Legend shown in Fig. 5b also applies to maps in Figs 5c, d, e, f, g and h. Refer to sample numbers on Fig. 2 for map locations. (a) Map of the southern Milly Milly area showing location of CS-491. (b) Map from the southwestern area showing location of sample CS0416. (c) Map from the central area showing location of sample CS0431. (d) Map from the northeastern area showing location of samples CS0394 and CS0395. (e) Map from the east-central area showing location of sample CS0377. (f) Map from the central area showing location of sample CS0392. (g) Map from the west-central area showing location of samples CS0371, CS0364, JAW-03-03 and CS0350. (h) Map from the west-central area showing location of sample CS0399. (d) Map from the northern Milly Milly area showing location of sample CS0341.

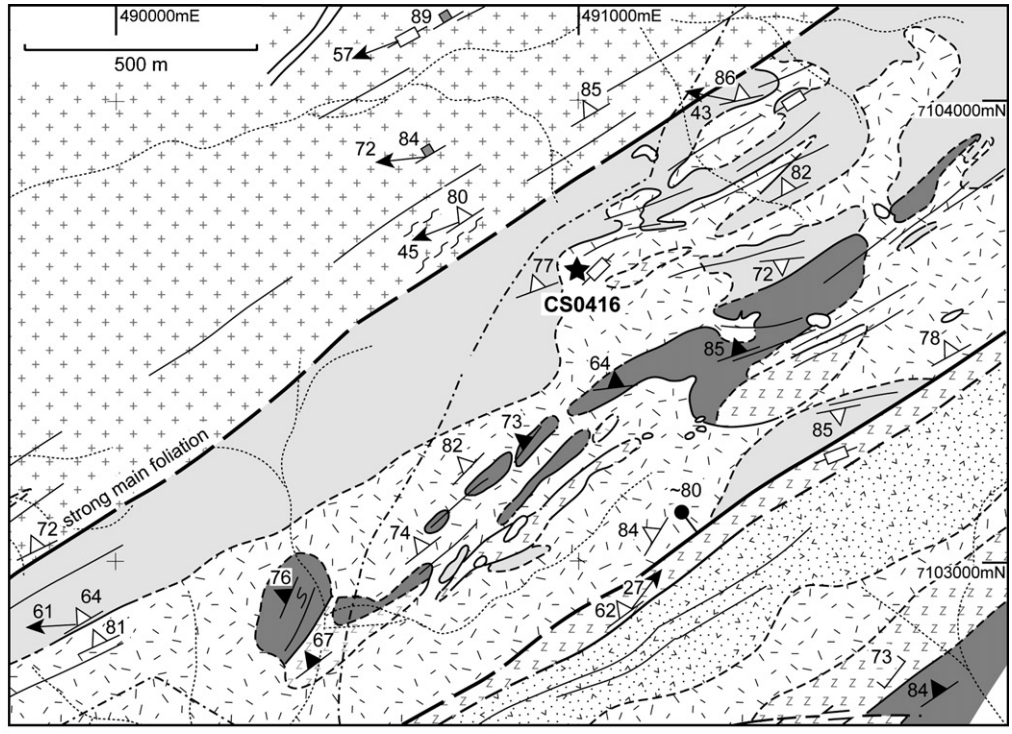

(b)

Dolerite plug, sill or dyke
Granitic dyke
Quartz veins
(Proterozoic) quartzite, metasandstone, metaconglomerate, quartz-mica schist, ferruginous schist
(Proterozoic) fine-grained micaceous schist, quartz-mica schist, quartzite
Muscovite granite and pegmatite, pegmatite
Granitic rocks
Fine-grained micaceous schist, quartz-mica schist, quartzite
Pebble metaconglomerate, interbedded with metagritstone, metasandstone, quartzite and fine-grained micaceous schist
Interbedded metasandstone, quartzite, metagritstone, minor pebble metaconglomerate, and fine-grained micaceous schist
Black and white ferruginous psammite, quartzite, jaspilitic chert, minor quartz-mica schist and metasandstone
Fine-grained micaceous schist, quartz-mica schist, quartzite, sometimes interleaved with mafic or ultramafic schist
Quartzite or chert (locally fuchsitic), black and white banded chert, jaspilite, minor quartz-mica schist, banded iron formation
Banded iron formation, chert
Mafic schist (mostly hbl or act-rich), chlorite-schist, often interleaved with quartz-mica or biotite schist, and ultramafic rocks
Serpentinised ultramafic rocks, silicified ultramafic rocks, mafic schist
Gneiss, foliated granitic rocks, pegmatite, mafic and ultramafic schist

Major fault with dip; inferred
Reverse or thrust fault with dip; inferred
Fault or unconformity, or both
Brittle or minor fault with dip; inferred
Lithological boundary; inferred
Axial trace of fold hinges
Trend lines of main foliation
Form lines of anastomosing foliation
Bedding; vertical; overturned
Early foliation; vertical
Compositional banding (BIF and chert); parallel to main foliation (Sm); vertical
Main foliation (S_m); vertical
Crenulation cleavage (Scc); vertical
Gneissic layering
Fold with axial surface and plunge
Antiform; synform
Mineral lineation (Lm)
Fold vergence (to next antiform) S_o/S_m

Creek
Track or road
Sample site

Fig. 5. (*Continued*).

lineation in the metabasaltic rocks that is parallel to moderately to steeply, predominantly south-plunging F_1 fold axes. These folds and foliations are overprinted by a northeast- or north-trending foliation and associated tight folds, which are particularly evident in the southeast, adjacent to the Carbar Fault (Figs. 3 and 4). This suggests that the deformation that produced the regional trend of the Meekatharra structural zone post-dates the northwest-trending structures in the Mingah Range greenstone belt, as does the truncation of both the Weld Range and Mingah Range greenstone belts by the Carbar Fault. These structures are all cut by the east- to east-northeast trending faults.

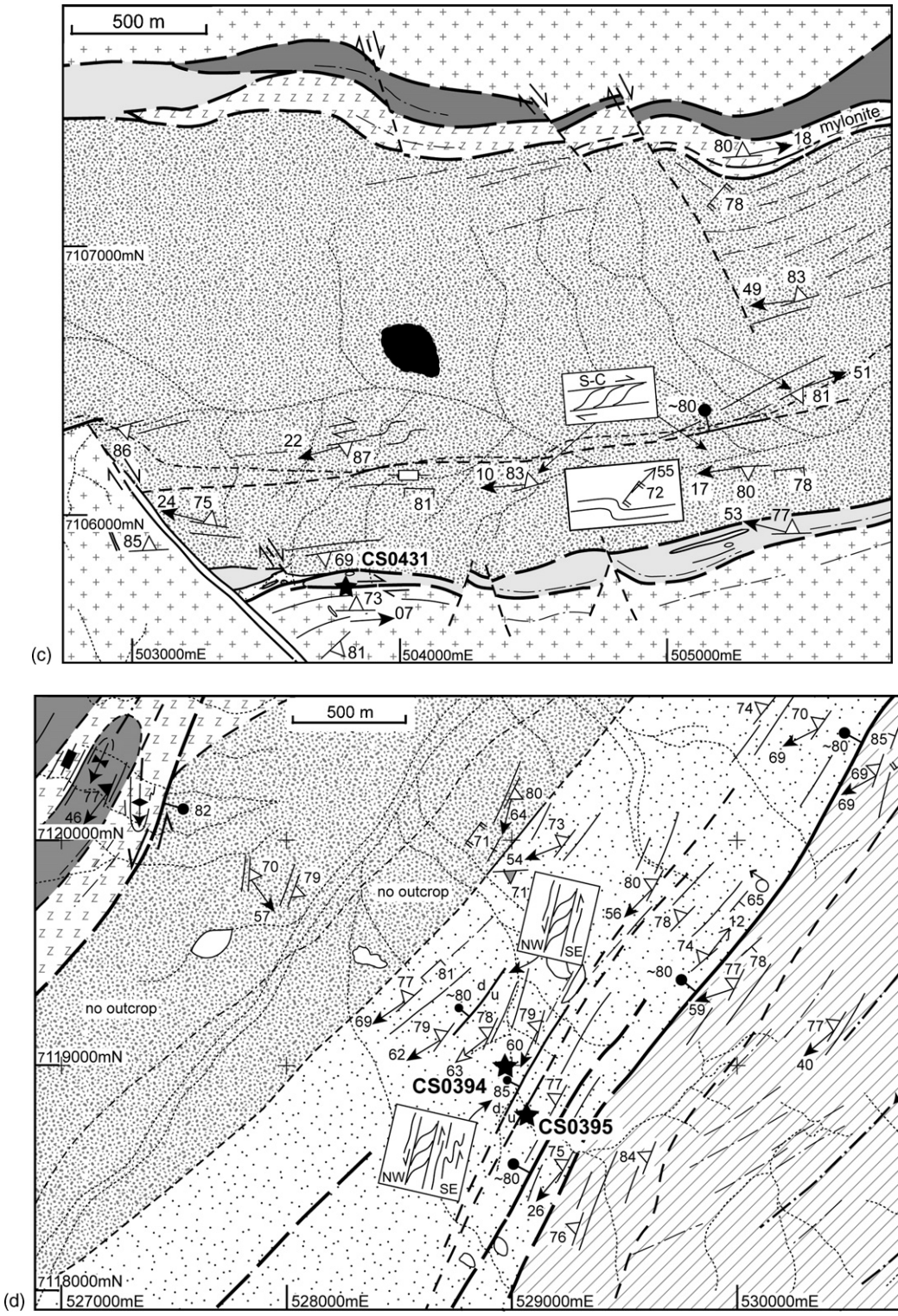

Fig. 5. (*Continued*).

The Yalgar Fault is an east-northeast-trending fault that has been interpreted as the terrane boundary between the Narryer Terrane and the Murchison Domain of the Youanmi Terrane (Myers, 1990a,b, 1993, 1997). It has been described as a zone of intense late Archean deformation, with intrusion of granite sheets, that was reactivated during the Proterozoic, and that is still active (Myers, 1990a, 1995, 1997). In new aeromagnetic data (Fig. 3), the eastern part of the Yalgar Fault is interpreted as a series of east-northeast-trending faults, similar to other east- to east-northeast-trending faults in the region (Spaggiari, 2006; Geological Survey of Western Australia, 2006), and cannot be readily defined as a major, continuous structure as shown in

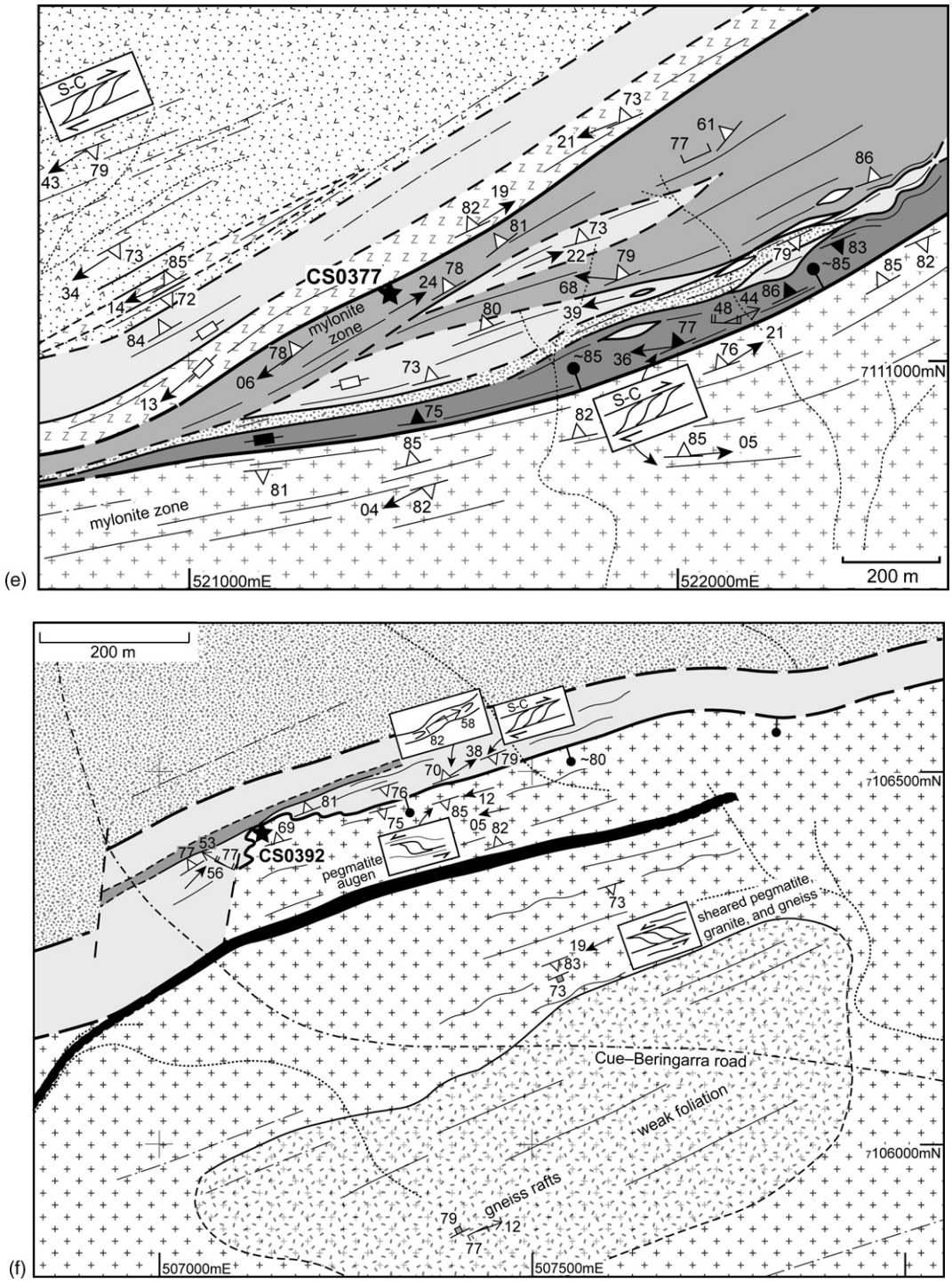

Fig. 5. (*Continued*).

Myers (1990a,b, 1995). In newly acquired gravity data (Fig. 4) the eastern part of the Yalgar Fault is not readily defined at all, whereas both the Carbar Fault and Chunderloo Shear Zone have strong signatures that correlate well with their positions shown in the aeromagnetic data (Fig. 3). This is due in part to the large density contrasts between granites and greenstones in the region. However, major structures such as reactivated terrane boundaries would normally be expected to have a gravity signature, even if it is a weak one. This, and the poor definition in the aeromagnetic data, suggest that the eastern part of the Yalgar Fault is not a major structure, as previously interpreted.

3. $^{40}Ar/^{39}Ar$ dating

A total of thirteen samples were dated using both IR laser step-heating and UV laser spot $^{40}Ar/^{39}Ar$ dating techniques (Table 1). Ten of the samples contained white micas from quartz-mica and andalusite schists, sheared pegmatite, granite, and

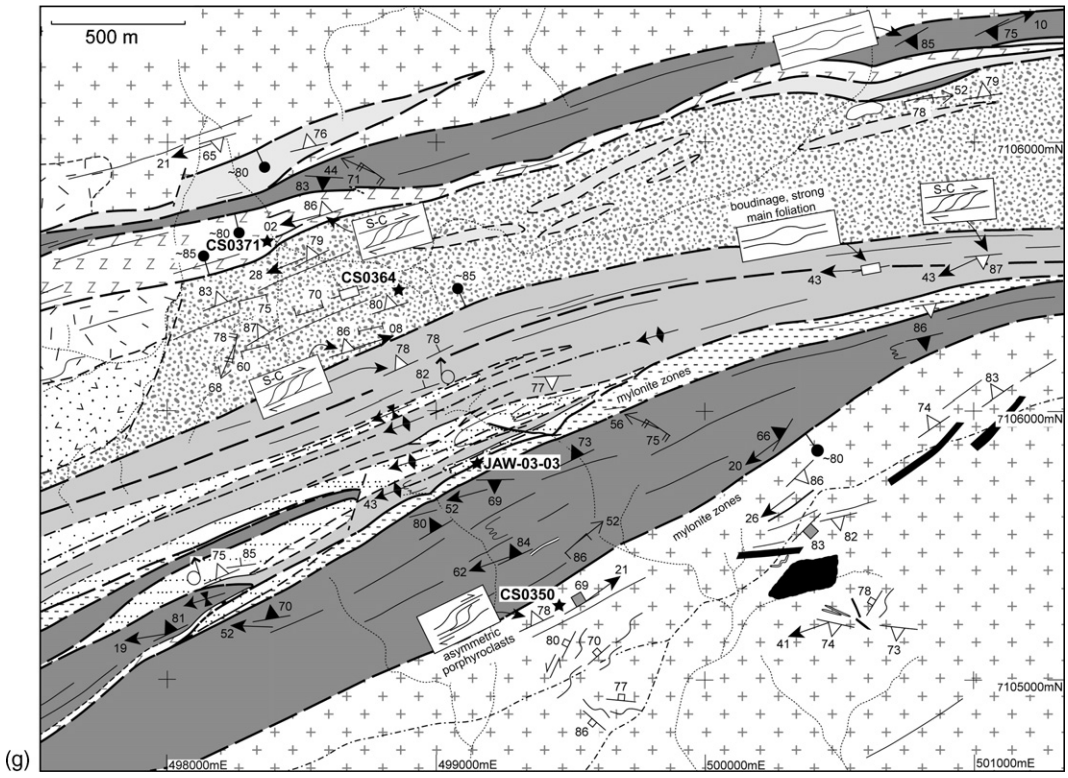

(g)

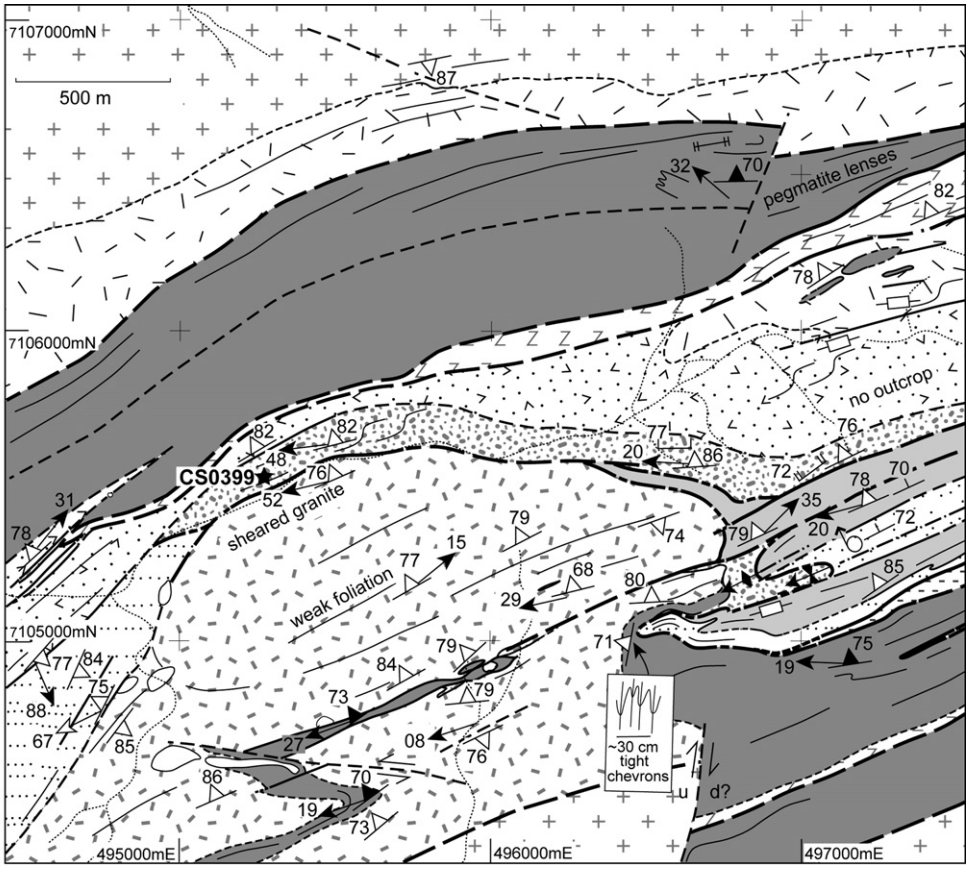

(h)

Fig. 5. (*Continued*).

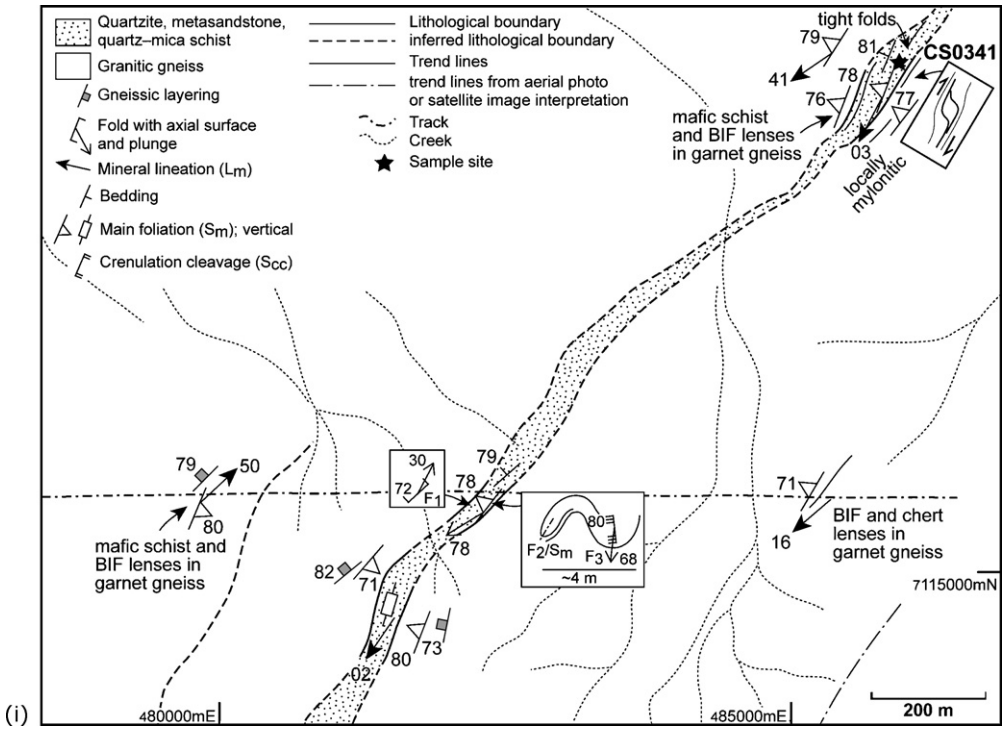

Fig. 5. (*Continued*).

granitic gneiss. Two samples contained biotite from a sheared granite and a quartz-biotite schist, and one sample contained hornblende from a mafic schist. The primary aim was to try to constrain the age of a major deformation and/or cooling event related to the formation of the Cargarah Shear Zone, by determining the cooling ages from the sheared rocks. The $^{40}Ar/^{39}Ar$ dating of these different minerals allows us to evaluate the medium-temperature thermal history of this region, owing to the unique Ar diffusion and Ar closure temperature properties of each mineral (i.e., hornblende, white mica and biotite). Most of the samples were collected from sheared rocks that appeared to be completely recrystallised, and contained only shear-related foliations that included fresh white mica, or biotite. Other samples, such as the pegmatites and granitic gneiss, were chosen to see if any different cooling ages were preserved, or whether the Jack Hills greenstone belt and surrounding rocks cooled uniformly. The samples were chosen to cover most areas of the belt, including the Milly Milly area (Fig. 2). The different techniques were chosen primarily according to material type, e.g., mineralogy and grain size. Where possible, *in situ* UV laser spot $^{40}Ar/^{39}Ar$ dating was undertaken on polished thick sections of schist samples to target micas in the main, shear-related foliation. Using different techniques also allowed some cross-checking of results. The experimental details of the techniques are described in Appendix A.

3.1. Sample descriptions and their relationship to structures in the Jack Hills region

3.1.1. Sample CS-491

Sample CS-491 is from a sliver of mafic schist within granitic gneiss from the western end of the Cargarah Shear Zone, in the Milly Milly area (Figs. 2 and 5a). The sample was collected by H. Zwingmann (CSIRO Petroleum Resources) for K–Ar dating of hornblende, which gave an age of 3248 ± 64 Ma (2σ, H. Zwingmann, written communication, 2004). It was chosen for dating by the $^{40}Ar/^{39}Ar$ technique to see whether this age could be repeated, because the K–Ar age is similar to the c. 3.3 Ga metamorphic SHRIMP U–Pb ages recorded in granitic gneisses of the Narryer Terrane (Nutman et al., 1991; Pidgeon and Wilde, 1998), and may indicate cooling from a thermal event at that time.

The area around the sample site is dominated by mylonite and ultramylonite zones with a steeply dipping, east-trending foliation and mostly shallowly west-plunging mineral lineation that shows local strong rodding (Fig. 5a). In areas of lower strain, the main foliation is axial planar to tight to isoclinal, steeply plunging folds. Porphyroclasts of K-feldspar commonly have dextral asymmetry, and dextral S–C fabrics are locally developed, although the latter sometimes show sinistral sense. The main foliation is locally overprinted by a crenulation cleavage. Pods of ultramafic rocks as well as mafic schists occur throughout, and the granitic gneisses locally show epidote alteration.

The sample consists of hornblende, plagioclase, biotite, Fe-oxide, minor chlorite and quartz (Fig. 6a; Table 1). The hornblende is pleochroic from yellow to blue–green, and has grown in aggregates, most likely replacing pyroxene, and is partially chloritised. Biotite is locally present along cleavage planes within hornblende, and also as small grains throughout the rock. Plagioclase laths are approximately 1 mm long and have an interlocking texture with relict grains of pyroxene. The mafic schist is interpreted as a metamorphosed dyke within orthogneiss.

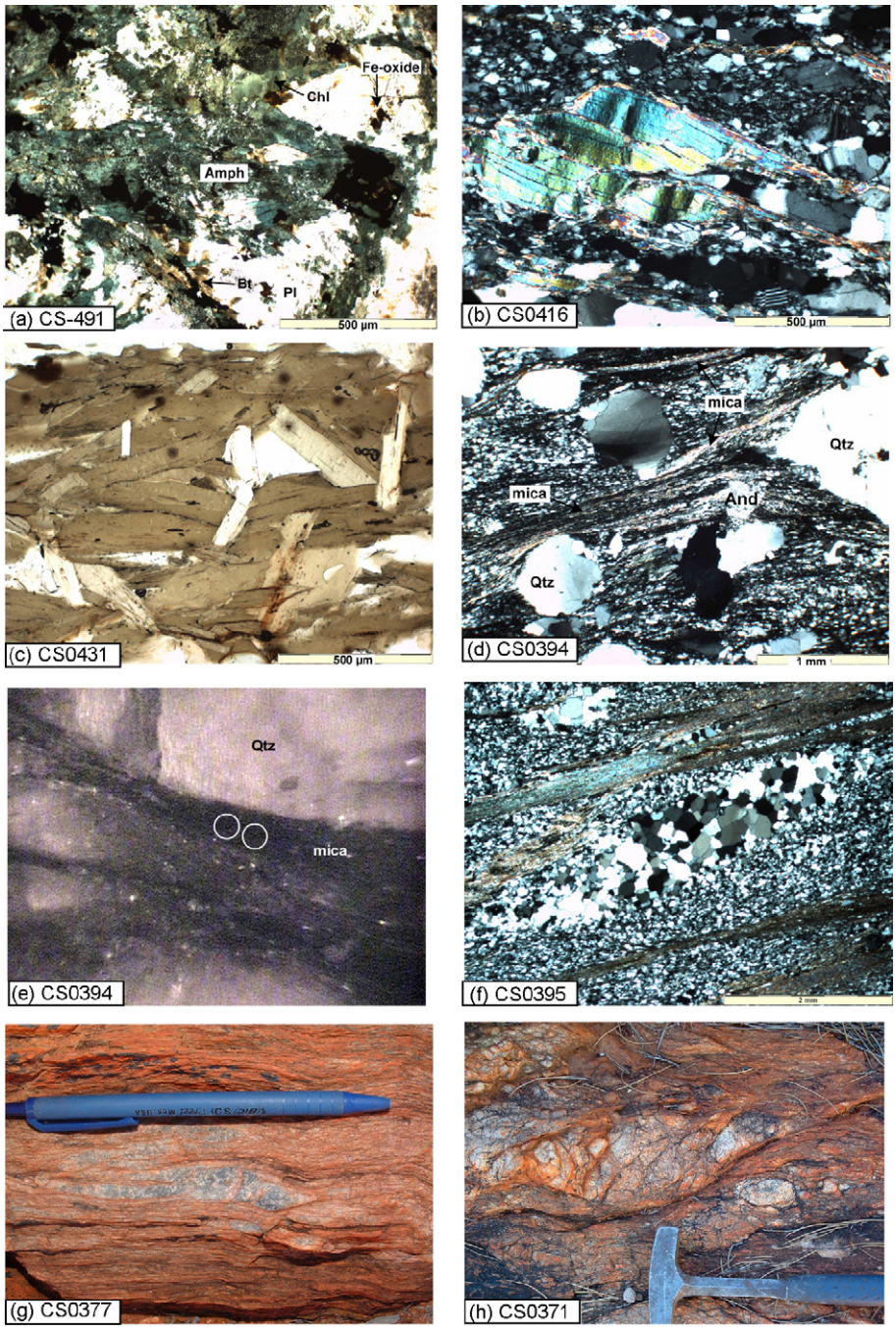

Fig. 6. (a) Photomicrograph, in plane-polarized light, of metadolerite schist sample CS-491 showing hornblende (Amph) growing in clusters, most likely replacing pyroxene (large mass in centre of photo). Small biotite (Bt) grains occur throughout. Other phases shown are plagioclase (Pl), Fe-oxide, and chlorite (Chl). (b) Photomicrograph, in cross-polarized light, of muscovite granite sample CS0416 showing typical muscovite grain, similar to that dated. The muscovite is kinked, and shows evidence of new, smaller grain growth parallel to the foliation on the right-hand side of the grain. Muscovite grains in the rock range from approximately 100 μm to 1 cm. (c) Photomicrograph, in plane-polarized light, of predominantly biotite grains from sheared granite (biotite schist) sample CS0431. Biotite laths have an average length of 500 μm, and are mostly fresh, although some show minor chloritisation. The strong foliation is defined by biotite (Bt) and quartz (Qtz). (d) Photomicrograph, in cross-polarized light, of quartz-mica schist sample CS0394, showing quartz (Qtz) and andalusite (And) porphyroblasts with micaceous and chloritic pressure shadows. (e) Photograph of part of a thick section chip from sample CS0394 taken with the high-resolution CCD camera fitted to the microscope during in situ UV laser ablation. The white circles annotate the 90 μm analysis spots within a band of fine-grained mica. (f) Photomicrograph, in cross-polarized light, of mylonitic quartz-mica schist sample CS0395. The strong mica fabric was targeted for *in situ* UV laser $^{40}Ar/^{39}Ar$ dating. (g) Isoclinally folded quartz veins in quartz-mica mylonite schist, where sample CS0377 was collected from. The pen shows the scale. (h) Deformed pegmatite in a semi-brittle fault zone in the northern part of the west-central area. Sample locality for CS0371. (i) Photomicrograph, in plane-polarized light, of quartz-biotite schist sample CS0364, showing strong biotite and quartz foliation. (j) Boudinaged quartz veins in Proterozoic quartz-mica schist, within the fault contact with the mature clastic association. Sample JAW-03-03 is from the boudin neck to the right of the quartz vein. (k) Granitic gneiss where sample CS0350 was collected from. The pen shows the scale. (l) Photomicrograph, in cross-polarized light, of granitic gneiss sample CS0350, showing foliation-forming white mica. (m) Photomicrograph, in cross-polarized light, of quartz-mica schist sample CS0341 showing white mica as the main foliation-defining mineral. Two generations of mica growth are indicated by the different grain sizes (central part of the photo).

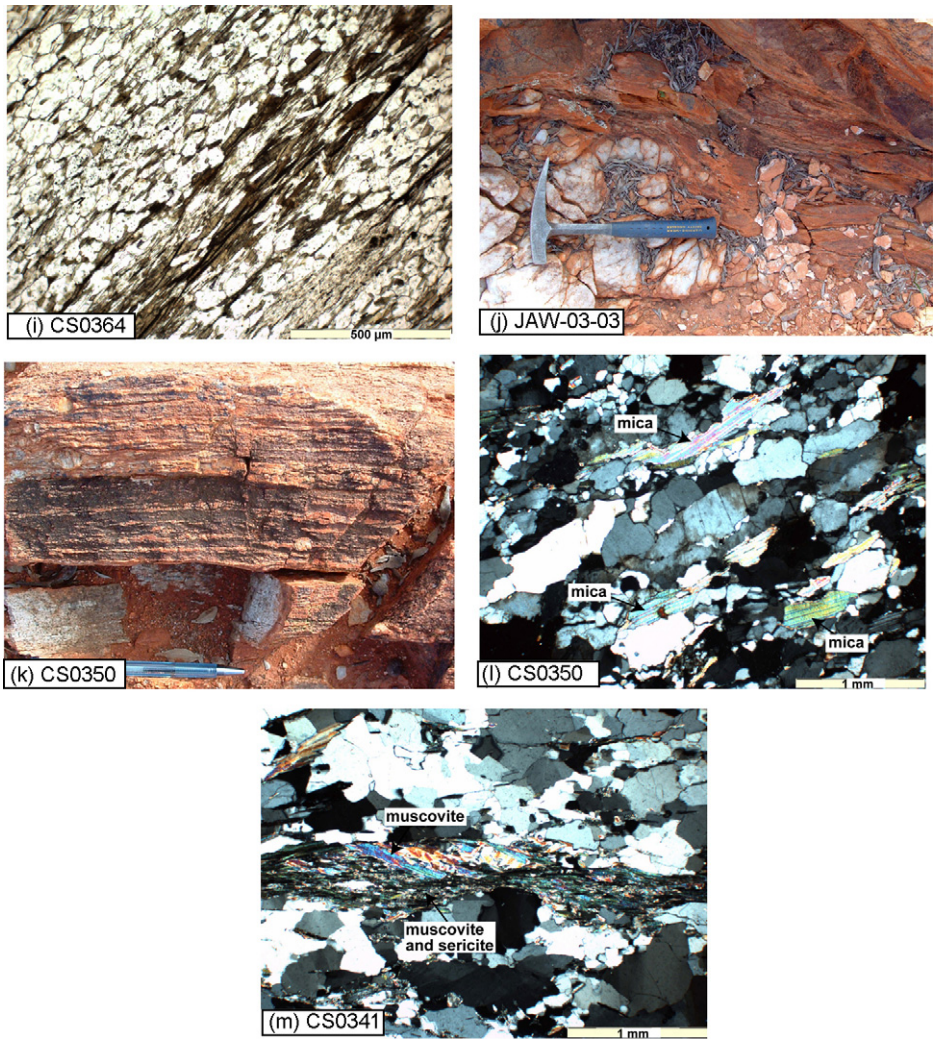

Fig. 6. (*Continued*).

3.1.2. Sample CS0416

Sample CS0416 is from foliated muscovite granite that intrudes metamorphosed BIF, chert and ultramafic rocks in the southwestern area (Figs. 2 and 5b ; Table 1). The main foliation in the area is northeast-trending and steeply dipping, and cuts the BIF, chert and ultramafic rocks as well as the granite. It is parallel to a major fault contact between granitic gneisses and predominantly mafic and ultramafic rocks, interpreted to be a fault splay from the Cargarah Shear Zone (Fig. 2). Locally, both the foliation and lenses of BIF and chert within the granite are folded into small-scale, tight folds.

The sample consists of quartz and twinned feldspar with an interlocking texture, and interstitial muscovite. Muscovite grains range from approximately 100 μm to 1 cm (Fig. 6b). The foliation is defined by zones of recrystallised feldspar and quartz that have undergone grain size reduction, and aligned white mica. The white mica was separated for $^{40}Ar/^{39}Ar$ dating by IR laser step-heating.

3.1.3. Sample CS0431

Sample CS0431 is a sheared granite from the east-trending fault contact with mafic and ultramafic schist on the southern margin of the central part of the belt, where it is cut by the Cargarah Shear Zone (Figs. 2 and 5c; Table 1). The contact is marked by mylonite zones with a medium to coarse micaceous foliation (targeted by the sampling) that is mostly developed in granite and pegmatite. Porphyroclasts indicate both dextral and sinistral movement, but the curvature of southwestward to eastward trend of the foliation from ∼100 m south into the fault contact suggests dextral fault movement (Fig. 5c). The fault contact is truncated by late, northwest-trending, brittle faults (see Plate 3, Spaggiari,2007a).

The sample contains a strong foliation defined by quartz and biotite (Fig. 6c). Relict grains of K-feldspar are locally preserved. Laths of K-feldspar aligned perpendicular to the foliation are kinked, indicative of shortening. Biotite laths have an average length of 500 μm, and are mostly fresh, although some show minor chloritisation. Quartz is elongate and exhibits undulose extinction, but, like most samples in the Jack Hills area, shows some evidence of recovery such as straight grain boundaries and foam-structure. The biotite was separated for $^{40}Ar/^{39}Ar$ dating by IR laser step-heating.

3.1.4. Samples CS0394 and CS0395

Samples CS0394 and CS0395 are from the northeastern part of the belt, adjacent to a major northeast-trending fault interpreted as a fault splay from the Cargarah Shear Zone (Figs. 2 and 5d; Table 1). The fault marks the contact between interpreted Proterozoic metasedimentary rocks and predominantly black and white ferruginous psammitic rocks, quartzite and metasandstone. Both sample locations are adjacent to steeply northwest-dipping minor faults that trend parallel to the main contact fault.

Sample CS0394 comes from a quartz–mica–andalusite schist with a strong micaceous foliation and small lenses of pulled apart or rodded quartz veins. The schist contains north- to northeast-trending, moderately south-plunging tight to isoclinal folds that are overprinted by the main foliation. In sample CS0394 the main foliation is defined by fine-grained quartz, white mica (targeted for $^{40}Ar/^{39}Ar$ dating by the *in situ* UV laser technique) and chlorite (Figs. 6d and e).

Sample CS0395 is from an outcrop of disrupted interbedded and veined quartzite and quartz-mica schist that has the appearance of a metaconglomerate, but is interpreted as a fault mélange because it has a variety of clast sizes in one ~8 m wide horizon adjacent to a fault. The sample is quartz-rich, with elongate aggregates of quartz up to ~1 to 2 cm, wrapped by a strong, fine-grained micaceous foliation, which was targeted for $^{40}Ar/^{39}Ar$ dating by the *in situ* UV laser technique (Fig. 6f). Andalusite occurs as small porphyroblasts and is also wrapped by the foliation.

3.1.5. Sample CS0377

Sample CS0377 comes from a quartz–mica–andalusite schist from the east-central part of the belt, near the southern fault contact with the granitic gneisses (Figs. 2 and 5e; Table 1). This is within the Cargarah Shear Zone, close to where it cuts the belt on the eastern side, and where fault splays are interpreted to extend to the northeast (see inset of Fig. 2). In this area, the metasedimentary schists are interleaved with metamorphosed ultramafic rocks, chert and BIF. Mylonite zones are common, and large-scale boudinaged lenses containing ultramafic rocks indicate stretching parallel to the margins of the belt (Fig. 5e).

Sample CS0377 contains quartz and andalusite porphyroblasts that are wrapped by a strong fine-grained micaceous foliation, which was targeted for $^{40}Ar/^{39}Ar$ dating by the *in situ* UV laser technique. The foliation is mylonitic and axial planar to isoclinally folded quartz veins (Fig. 6g).

3.1.6. Sample CS0392

Sample CS0392 is a sheared pegmatite from the central part of the belt, which is coincident with the Cargarah Shear Zone (Figs. 2 and 5f; Table 1). This area is dominated by high-strain, boudinage, tight to isoclinal folds, and predominantly dextral S-C foliations and kinematic indicators (Spaggiari, 2007a). The main foliation is steeply dipping, and is locally folded by northeast-trending upright folds. Mylonite is locally developed, particularly in BIF, chert, and quartzite on the northern margin. The mineral lineation plunges shallowly to moderately, either to the east or west. South of the southern margin of the belt relatively undeformed domes and tors of monzogranite are transitional into strongly deformed and sheared granite and pegmatite, near the contact with mafic and ultramafic rocks (Fig. 5f). The sample comes from one of these sheared pegmatites, which contains coarse white mica that was targeted for UV laser spot $^{40}Ar/^{39}Ar$ dating. The contact is a steeply dipping shear zone with complex small-scale folds and both sinistral and dextral kinematic indicators, and includes stretched lenses of BIF and chert within the mafic and ultramafic rocks.

3.1.7. Samples CS0371, CS0364, JAW-03-03 and CS0350

Samples CS0371, CS0364, JAW-03-03 and CS0350 all come from the west-central area (Figs. 2 and 5g; Table 1). The Cargarah Shear Zone cuts through gneiss and granitic rocks to the north of the belt in this area, and merges with southwest-trending fault splays (see inset in Fig. 2). Mylonitisation associated with the shearing increases to the east, but local high strain zones with predominantly dextral S-C foliations are common throughout. These fabrics cross-cut moderately southwest-plunging, open to tight inclined folds, predominantly developed in mature clastic rocks to the south (Spaggiari, 2007a,b). Small, late-stage brittle faults and kink folds overprint the main foliation.

Sample CS0371 is from a deformed pegmatite from close to the northern fault contact of the belt (Figs. 5g and 6h; Table 1). BIF, chert, quartzite strike ridges and lenses of mafic and ultramafic rocks define the northern margin of the belt in this area, and are intruded by muscovite granite. The main foliation dips steeply to the east or west and mineral lineations mostly have shallow plunges to the west. Dextral S-C fabrics and intrafolial isoclinal folds occur locally. Several ~10 m wide semi-brittle fault zones that contain fault breccia and cataclasite overprint the main foliation. The sample was collected from one of these, in order to determine the age of cooling and/or late-stage deformation. It contained coarse-grained white mica that was targeted for UV laser spot $^{40}Ar/^{39}Ar$ dating.

Sample CS0364 is a quartz-biotite schist from a section of strongly deformed pelitic and semipelitic rocks that are in fault contact with mature clastic rocks to the south, and BIF, chert and ultramafic rocks to the north (Fig. 5g; Table 1). The sequence contains an early foliation that is overprinted by the dominant, strong, east northeast-trending subvertical foliation. This is locally overprinted by a northwest- or northeast-trending crenulation cleavage. Dextral S-C fabrics occur locally. The sample has a strong, fine-grained foliation defined by quartz and biotite, which was targeted for $^{40}Ar/^{39}Ar$ dating by the *in situ* UV laser technique (Fig. 6i).

Sample JAW-03-03 is a fine-grained quartz-mica schist from a ~0.5 m wide, east-northeast trending semi-brittle fault zone that is interpreted as a contact between Proterozoic rocks to the south and mature clastic rocks to the north (Figs. 5g and 6j; Table 1; Spaggiari, 2007a). The fault zone cuts the main foliation in rocks on either side, and contains a strong foliation, small duplexes that suggest sinistral displacement, quartz veins, northwest-trending kinks, and local tight folds parallel to the fault boundaries. It has a sharp, irregular contact with the mature clastic rocks and may be either a reactivated structure, or a late structure formed after the main phase of shearing. The sam-

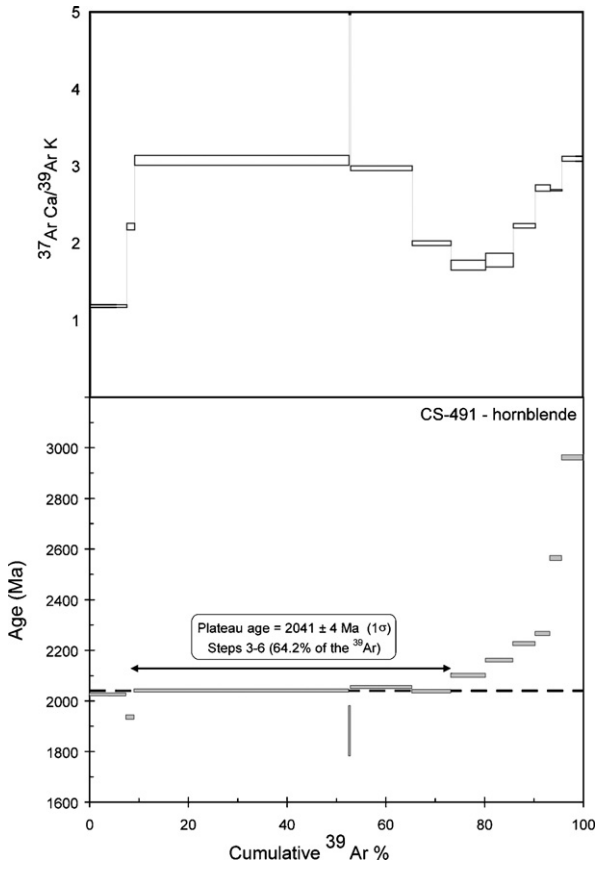

Fig. 7. Sample CS-491 (hornblende) $^{40}Ar/^{39}Ar$ age spectrum and $^{37}Ar_{Ca}/^{39}Ar_K$ versus cumulative % ^{39}Ar plot. Individual errors are 1σ (denoted by the box height on the age spectrum).

ple is dominated by quartz and sericitic white mica, which was targeted for UV laser spot $^{40}Ar/^{39}Ar$ dating.

Sample CS0350 is a granitic gneiss that was sampled close to the fault contact with BIF along the southern margin of the belt (Figs. 5g and 6k; Table 1). This margin is a steeply-dipping shear zone that trends parallel to the belt. The BIF is internally folded with tight to isoclinal, mostly second generation folds. These are locally refolded into tight folds, parallel to the trend of the belt. The granitic gneiss contains a gneissic banding that is similarly oriented to the main, overprinting foliation. Mylonite zones occur locally within the granitic rocks and gneiss, and contain both symmetric and dextral K-feldspar porphyroclasts. Near sample site CS0350, north-trending quartz veins cut the main foliation, as do small northeast-trending brittle faults. The sample contains quartz, K-feldspar, biotite, white mica and garnet. The medium- to coarse-grained white mica occurs within the foliation (Fig. 6l), and was targeted for $^{40}Ar/^{39}Ar$ dating by the *in situ* UV laser technique.

3.1.8. Sample CS0399

Sample CS0399 is a quartz-mica schist from the west-central part of the belt Figs. 2 and 5h; Table 1). The quartz-mica schist is the western extension of the same band of pelitic to semipelitic schist from which CS0364 was sampled. It wraps around the margin of an intrusion of late Archean monzogranite, known as 'the Blob', that intruded the pelitic to semipelitic schist (Spaggiari, 2007a). The granite is predominantly weakly foliated, but sheared and locally folded at its margins. The quartz-mica schist is also sheared in this area. Both the granite and the quartz-mica schist contain a steeply northwest-dipping foliation and mineral lineation that plunges moderately to steeply to the southwest (Fig. 5h). Lenses of sheared and boudinaged granite and pegmatite occur in the quartz-mica schist. The sample contains a strong foliation defined by fine-grained quartz and white mica, which was targeted for $^{40}Ar/^{39}Ar$ dating by the *in situ* UV laser technique.

3.1.9. Sample CS0341

Sample CS0341 is a quartz-mica schist from the northern part of the Milly Milly area (Figs. 2 and 5i; Table 1). It comes from the northern end of a series of lenses of predominantly metasedimentary rocks, mafic schist, BIF and chert within gneiss and granite. These lenses are interpreted to occur within fault splays off the western end of the Cargarah Shear Zone (see inset in Fig. 2), and locally contain zones of complexly refolded folds. The sample comes from a sequence of interbedded quartzite, quartz-mica schist, and metasandstone that contain a strong foliation that is subparallel to the bedding. This is locally overprinted by a north-trending, spaced foliation. Sample CS0341 contains quartz, muscovite, sericite, and minor chlorite. The foliation is defined by medium- to coarse-grained quartz and white mica,

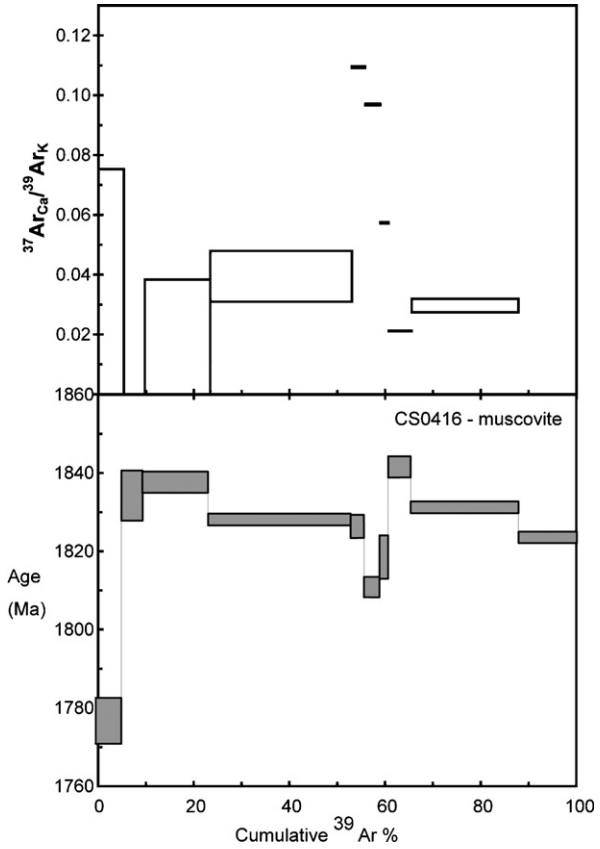

Fig. 8. Sample CS0416 (muscovite) $^{40}Ar/^{39}Ar$ age spectrum and $^{37}Ar_{Ca}/^{39}Ar_K$ versus cumulative % ^{39}Ar plot. Individual errors are 1σ (denoted by the box height on the age spectrum).

Table 2
$^{40}Ar/^{39}Ar$ results of samples dated by the IR laser step-heating method

Analysis	Age (Ma)	±	$^{40}Ar^*/^{39}Ar$	±	$^{40}Ar/^{39}Ar$	±	$^{38}Ar/^{39}Ar$	±	$^{37}Ar/^{39}Ar$	±	$^{36}Ar/^{39}Ar$	±	$^{36}Ar/^{40}Ar$	±	^{39}Ar (cm^3)	±	% $^{40}Ar^*$	Cumulative % ^{39}Ar
CS-491 hornblende[a]																		
Analysis 1	2021.7	6.4	97.49	0.16	99.58	0.16	0.01427	0.00079	1.18350	0.01816	0.00708	0.00001	0.00007	0.00000	6.41E−12	1.03E−14	97.9	7.55
Analysis 2	1932.0	8.7	90.47	0.49	92.61	0.50	0.02256	0.00390	2.21432	0.04158	0.00724	0.00004	0.00008	0.00000	1.30E−12	6.97E−15	97.7	9.08
Analysis 3	2036.6	6.5	98.68	0.18	99.54	0.17	0.01649	0.00017	3.07417	0.06492	0.00288	0.00020	0.00003	0.00000	3.69E−11	4.74E−14	99.1	52.60
Analysis 4	1878.8	99.5	86.47	7.36	104.01	1.52	0.03129	0.01840	7.59965	2.63481	0.05937	0.02454	0.00057	0.00024	2.76E−13	3.78E−15	83.1	52.93
Analysis 5	2051.0	6.8	99.86	0.25	100.76	0.23	0.01728	0.00004	2.97223	0.03018	0.00308	0.00032	0.00003	0.00000	1.06E−11	2.39E−14	99.1	65.40
Analysis 6	2034.3	7.4	98.50	0.34	99.54	0.31	0.01696	0.00005	1.99922	0.03152	0.00352	0.00050	0.00004	0.00001	6.71E−12	2.06E−14	99.0	73.31
Analysis 7	2097.8	7.6	103.72	0.36	104.35	0.26	0.01563	0.00004	1.71616	0.06355	0.00211	0.00085	0.00002	0.00001	5.96E−12	1.44E−14	99.4	80.34
Analysis 8	2158.3	7.5	108.87	0.35	108.87	0.14	0.01525	0.00002	1.77891	0.08820	0.00000	0.00000	0.00000	0.00000	4.75E−12	6.09E−15	100.0	85.93
Analysis 9	2222.8	8.1	114.54	0.45	115.57	0.43	0.01645	0.00090	2.22532	0.02873	0.00346	0.00045	0.00003	0.00000	3.78E−12	1.39E−14	99.1	90.38
Analysis 10	2262.6	7.3	118.16	0.31	118.93	0.24	0.01216	0.00187	2.71554	0.04104	0.00262	0.00066	0.00002	0.00001	2.55E−12	4.78E−15	99.3	93.39
Analysis 11	2562.7	9.6	148.07	0.73	148.83	0.55	0.01498	0.00163	2.68722	0.00980	0.00258	0.00163	0.00002	0.00001	2.07E−12	7.56E−15	99.5	95.84
Analysis 12	2961.4	10.4	196.37	1.00	198.11	0.97	0.01562	0.00096	3.09503	0.03310	0.00591	0.00096	0.00003	0.00000	3.53E−12	1.72E−14	99.1	100.00
CS0416 muscovite[b]																		
Analysis 1	1776.6	8.2	79.03	0.41	79.38	0.22	0.01233	0.00106	0.00950	0.06579	0.00118	0.00118	0.00001	0.00001	5.73E−12	1.59E−14	99.6	5.34
Analysis 2	1834.1	8.6	83.12	0.46	83.33	0.19	0.01278	0.00107	0.00000	0.00000	0.00072	0.00143	0.00001	0.00002	4.72E−12	1.08E−14	99.7	9.74
Analysis 3	1837.5	6.4	83.37	0.20	83.47	0.10	0.01246	0.00033	0.01857	0.01980	0.00034	0.00058	0.00000	0.00001	1.47E−11	1.69E−14	99.9	23.41
Analysis 4	1827.9	5.9	82.68	0.11	82.75	0.07	0.01194	0.00015	0.03945	0.00849	0.00026	0.00027	0.00000	0.00000	3.18E−11	2.57E−14	99.9	53.03
Analysis 5	1826.2	6.4	82.55	0.21	82.55	0.21	0.01153	0.00113	0.10938	0.00028	0.00000	0.00000	0.00000	0.00000	2.99E−12	7.56E−15	100.0	55.81
Analysis 6	1810.7	6.3	81.44	0.18	81.44	0.18	0.01225	0.00100	0.09689	0.00022	0.00000	0.00000	0.00000	0.00000	3.38E−12	7.56E−15	100.0	58.96
Analysis 7	1818.4	8.0	81.99	0.40	82.77	0.30	0.01449	0.00005	0.05736	0.00021	0.00265	0.00089	0.00003	0.00001	1.90E−12	6.97E−15	99.1	60.74
Analysis 8	1841.4	6.4	83.65	0.19	83.74	0.17	0.01270	0.00003	0.02117	0.00004	0.00032	0.00033	0.00000	0.00000	5.16E−12	1.03E−14	99.9	65.54
Analysis 9	1831.1	5.9	82.90	0.10	82.98	0.10	0.01331	0.00016	0.02964	0.00226	0.00027	0.00014	0.00000	0.00000	2.40E−11	2.73E−14	99.9	87.88
Analysis 10	1823.4	5.9	82.35	0.10	82.35	0.07	0.01286	0.00013	0.00000	0.00000	0.00000	0.00000	0.00000	0.00000	1.30E−11	1.07E−14	100.0	100.00
CS0431 biotite[c]																		
Grain 1																		
Analysis 1	1869.2	6.3	85.72	0.18	85.72	0.15	0.01187	0.00030	0.00000	0.00000	0.00000	0.00000	0.00000	0.00000	5.67E−12	1.01E−14	100.0	20.91
Analysis 2	1813.5	6.4	81.68	0.20	81.68	0.17	0.00888	0.00035	0.00000	0.00000	0.00000	0.00000	0.00000	0.00000	4.85E−12	1.01E−14	100.0	38.82
Analysis 3	1818.2	6.6	82.02	0.23	82.01	0.23	0.01058	0.00003	0.06197	0.03067	0.00000	0.00000	0.00000	0.00000	3.59E−12	1.01E−14	100.0	52.04
Analysis 4	1813.9	6.1	81.71	0.16	81.71	0.16	0.01203	0.00002	0.03144	0.01037	0.00000	0.00000	0.00000	0.00000	1.06E−11	2.03E−14	100.0	91.17
Analysis 5	1827.5	7.3	82.69	0.32	82.68	0.32	0.01404	0.00005	0.07550	0.02491	0.00000	0.00000	0.00000	0.00000	2.21E−12	8.45E−15	100.0	99.33
Analysis 6	1841.8	38.9	83.72	2.79	83.72	2.79	0.00000	0.00000	0.00000	0.00000	0.00000	0.00000	0.00000	0.00000	1.83E−13	6.09E−15	100.0	100.00
Grain 2																		
Analysis 2-1	1805.8	5.9	81.13	0.11	81.13	0.11	0.01298	0.00071	0.00000	0.00000	0.00000	0.00000	0.00000	0.00000	4.78E−12	6.09E−15	100.0	7.97
Analysis 2-2	1813.9	5.9	81.71	0.09	81.71	0.09	0.01297	0.00019	0.00000	0.00000	0.00000	0.00000	0.00000	0.00000	2.47E−11	2.75E−14	100.0	49.22
Analysis 2-3	1806.6	5.7	81.19	0.05	81.19	0.05	0.01316	0.00015	0.00000	0.00000	0.00000	0.00000	0.00000	0.00000	2.50E−11	1.36E−14	100.0	90.95
Analysis 2-4	1824.8	6.5	82.49	0.23	82.49	0.21	0.01556	0.00031	0.00000	0.00000	0.00000	0.00000	0.00000	0.00000	5.43E−12	1.36E−14	100.0	100.00

[a] 1σ errors; J value = 0.021200 ± 0.000106; irradiation standard used = Tinto B biotite (409.24 ± 0.71 Ma).
[b] 1σ errors; J value = 0.021221 ± 0.000106; irradiation standard used = Tinto B biotite (409.24 ± 0.71 Ma).
[c] 1σ errors; J value = 0.021210 ± 0.000106; irradiation standard used = Tinto B biotite (409.24 ± 0.71 Ma).

with fine-grained sericite interpreted as locally overgrowing the muscovite (Fig. 6m). The micas in the foliation were targeted for $^{40}Ar/^{39}Ar$ dating by the *in situ* UV laser technique.

3.2. Results

3.2.1. $^{40}Ar/^{39}Ar$ IR laser step-heating of mineral separates and individual grains

Six grains of hornblende from mafic schist sample CS-491 were dated. The average grain size of the IR laser step-heated sample was 300 × 150 μm, the largest grain was 370 × 240 μm, and the smallest grain was 170 × 160 μm. The hornblende sample produced a disturbed age spectrum (Fig. 7, Table 2). The first six steps yielded apparent ages ranging from 2051 to 1932 Ma, and yielded a plateau age of 2041 ± 4 Ma (1σ, mean squares of deviates (MSWD) = 2.0) for steps 3–6 with 64.2% of the total ^{39}Ar released. The remaining six steps show a gradual increase in age to the highest temperature age of 2961.4 ± 10.4 Ma (1σ). Step 4 (1878.76 ± 99.55 Ma (1σ)) has a large uncertainty reflecting the small amount of gas released during this step.

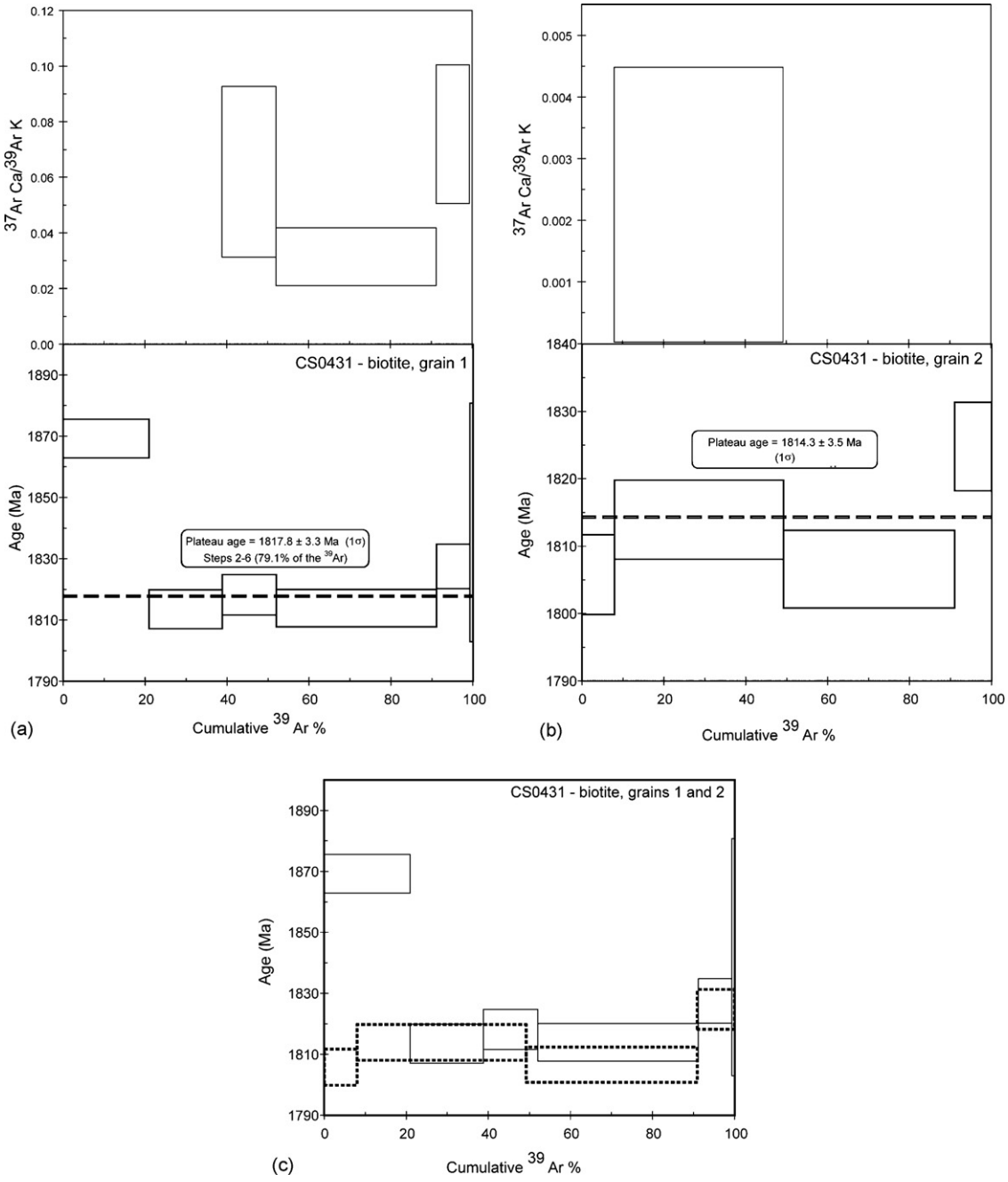

Fig. 9. (a) $^{40}Ar/^{39}Ar$ age spectrum and $^{37}Ar_{Ca}/^{39}Ar_K$ versus cumulative % ^{39}Ar plot for biotite grain 1, sample CS0431. Individual errors are 1σ (denoted by the box height on the age spectrum). Steps 2 through 6 gave a plateau age of 1817.8 ± 3.3 Ma (1σ), representing 79.1% of the ^{39}Ar released. (b) $^{40}Ar/^{39}Ar$ age spectrum for biotite grain 2, sample CS0431. Individual errors are 1σ (denoted by the box height on the age spectrum). Steps 2–4 yielded a plateau age of 1814.3 ± 3.5 Ma (1σ), representing 92% of the ^{39}Ar released. (c) $^{40}Ar/^{39}Ar$ age spectra from both biotite grains (1 and 2) from sample CS0431.

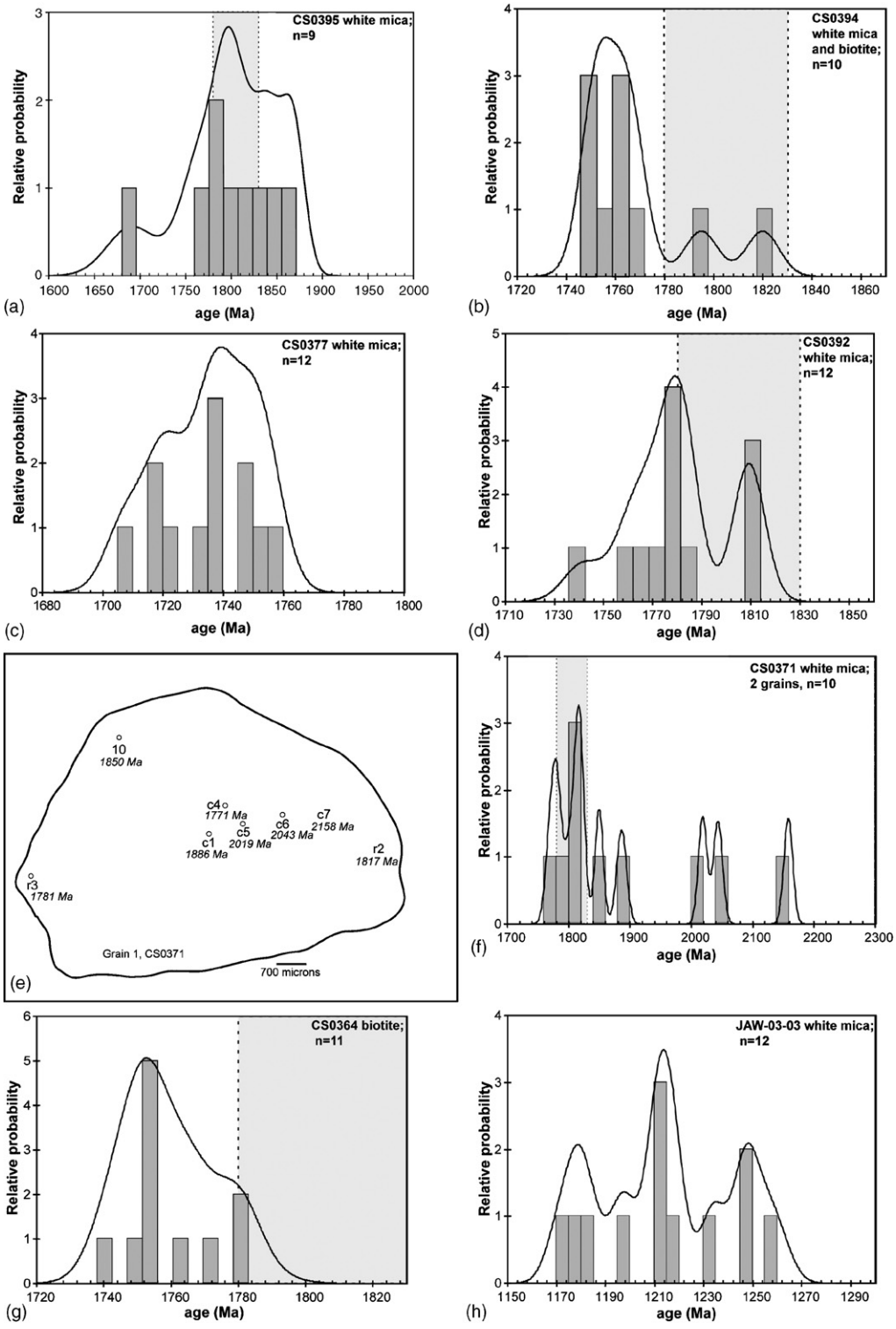

Fig. 10. (a) Probability density plot of all UV laser $^{40}Ar/^{39}Ar$ white mica ages for sample CS0395. Dashed shaded box denotes the 1830–1780 Ma Capricorn Orogeny. (b) Probability density plot of all UV laser $^{40}Ar/^{39}Ar$ white mica ages for sample CS0394. Dashed shaded box denotes the 1830–1780 Ma Capricorn Orogeny. (c) Probability density plot of all UV laser $^{40}Ar/^{39}Ar$ white mica ages for sample CS0377. (d) Probability density plot of all UV laser $^{40}Ar/^{39}Ar$ white mica ages for sample CS0392. Dashed shaded box denotes the 1830–1780 Ma Capricorn Orogeny. (e) Sketch of UV laser $^{40}Ar/^{39}Ar$ analysis points of white mica grain 1 from sample CS0371. (f) Probability density plot of all UV laser $^{40}Ar/^{39}Ar$ white mica ages for sample CS0371. Dashed shaded box denotes the 1830–1780 Ma Capricorn Orogeny. (g) Probability density plot of all UV laser $^{40}Ar/^{39}Ar$ white mica ages for sample CS0364. Dashed shaded box denotes the 1830–1780 Ma Capricorn Orogeny. (h) Probability density plot of all UV laser $^{40}Ar/^{39}Ar$ white mica ages for sample JAW-03-03. (i) Probability density plot of all UV laser $^{40}Ar/^{39}Ar$ white mica ages for sample CS0350. (j) Probability density plot of all UV laser $^{40}Ar/^{39}Ar$ white mica ages for sample CS0399. Dashed shaded box denotes the 1830–1780 Ma Capricorn Orogeny. (k) Probability density plot of all UV laser $^{40}Ar/^{39}Ar$ white mica ages for sample CS0341. Dashed shaded box denotes the 1830–1780 Ma Capricorn Orogeny.

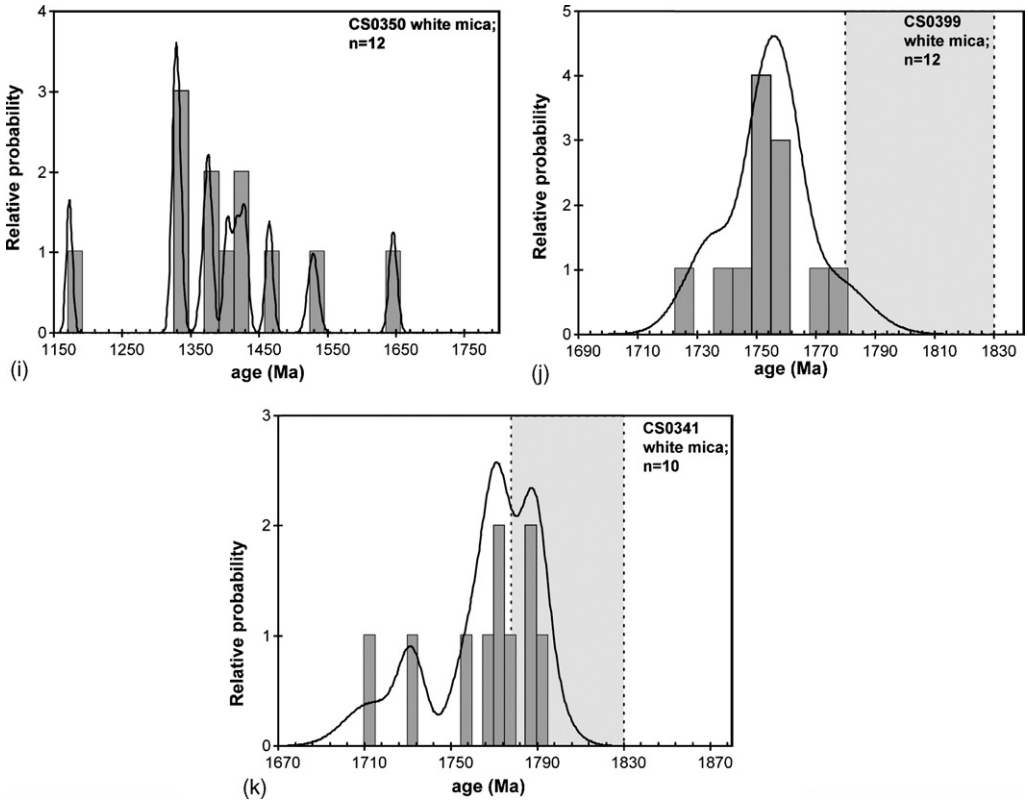

Fig. 10. (*Continued*).

The complexity in the data may be due, in part, to the growth of biotite along cleavage planes in the hornblende grains, in which case the apparent ages would reflect a mixture of two phases. Biotite and hornblende have different Ar closure temperatures. For example, we calculated the Ar closure temperatures for the hornblende and biotite in this sample to be 510 °C and 280 °C, respectively, using average grain diameters of 200 and 40 μm, Ar diffusion parameters of Harrison (1981) and Grove and Harrison (1996), spherical and cylindrical diffusion geometries, respectively, an estimated cooling rate of 10 °C/Ma, and employing the closure temperature equation of Dodson (1973). Therefore, these two phases would have retained different ages in a medium- to slow-cooling terrane. However, the observed variations in the $^{37}Ar_{Ca}/^{39}Ar_K$ ratios from 1.184 to 3.095 (excluding the anomalous small step 4) do not coincide with the variation in ages (Fig. 7), and is not typical for mixed biotite-hornblende samples (Rex et al., 1993). Therefore, this effect may be minimal. The progressive increase in apparent ages during laser step-heating may also reflect either the degassing of younger components from the grain rims (released at low temperatures), and older components from the grain cores (released at higher temperatures) (e.g., Harrison and McDougall, 1980). However, it may also be an artefact caused by phase changes in the amphibole grains that occurs during the vacuum step-heating process (e.g., Lee et al., 1991; Lee, 1993; Wartho et al., 1991). Excess ^{40}Ar may also be a contributing factor to the complexity of the results, although excess ^{40}Ar in hornblende typically yields U-shaped age spectra (e.g., Wartho et al., 1996). K–Ar dating of this hornblende sample yielded an older age of 3248 ± 64 Ma (2σ, H. Zwingmann, written communication, 2004), which is c. 280 million years older than the oldest $^{40}Ar/^{39}Ar$ step age of 2961.4 ± 10.4 Ma (1σ). This discrepancy may be due to either the heterogeneous presence of excess ^{40}Ar, or the heterogeneous partial degassing of $^{40}Ar^*$ in the grains. However, excess ^{40}Ar (i.e., ^{40}Ar found within a mineral that is in excess of the *in situ* produced $^{40}Ar^*$) in hornblende samples is almost universally recognised as yielding U-shaped step-heating age spectra with old ages at both the low- and high-temperature steps, which is not observed in sample CS-491. One hypothesis for the complexity of $^{40}Ar/^{39}Ar$ ages in this hornblende sample, is that the highest temperature age of 2961.4 ± 10.4 Ma (1σ) may reflect a minimum age for an older event, whilst the low-temperature plateau age of 2041 ± 4 Ma (1σ) may reflect a resetting or partial resetting age. These types of hornblende age spectra have been found in previous studies in another Western Australian greenstone belt, and have been interpreted as reflecting partial Ar resetting (e.g., Kent and McCuaig, 1997).

One muscovite grain from muscovite granite sample CS0416 yielded apparent ages between 1837 and 1776 Ma (Fig. 8, Table 2). Even though the spread of apparent ages is less than for hornblende sample CS-491, the age spectrum is disturbed and does not define a plateau age. This is most likely due to partial resetting within different domains of the muscovite grain. However, excluding the youngest age in step 1, a weighted mean of steps 2–10 yielded an age of 1827.7 ± 5.8 Ma (95% confidence, MSWD = 13). The lack of an age plateau may be due to the presence of multiple phases, as steps 5 and 6 contain higher $^{37}Ar_{Ca}/^{39}Ar_K$ ratios, indicating the possible degassing of

Table 3
$^{40}Ar/^{39}Ar$ results of samples dated by the UV laser *in situ* method

Analysis	Age (Ma)	±	$^{40}Ar^*/^{39}Ar$	±	$^{40}Ar/^{39}Ar$	±	$^{38}Ar/^{39}Ar$	±	$^{37}Ar/^{39}Ar$	±	$^{36}Ar/^{39}Ar$	±	^{39}Ar (cm^3)	±	% $^{40}Ar^*$
CS0395 white mica; in situ[a]															
Mica 1-1	1787.9	29.8	80.14	2.06	80.30	1.22	0.01976	0.00847	3.08980	1.04700	0.00000	0.00000	5.99E−13	3.78E−15	100.0
Mica 1-2	1690.5	26.7	73.44	1.75	82.15	1.04	0.01683	0.00721	3.74933	0.89212	0.02789	0.00481	7.03E−13	3.78E−15	89.6
Mica 3-2	1808.6	21.1	81.61	1.45	83.54	0.34	0.01437	0.00160	0.79547	0.05313	0.00619	0.00479	2.12E−12	8.45E−15	97.7
Mica 3-3	1789.5	32.2	80.26	2.24	83.26	0.38	0.00997	0.00249	0.99345	0.08291	0.00972	0.00748	1.36E−12	6.09E−15	96.5
Mica 3-4	1763.4	20.4	78.43	1.36	81.82	0.30	0.02033	0.00006	1.12632	0.15022	0.01101	0.00452	1.50E−12	4.78E−15	95.9
Mica 1-3	1847.4	17.0	84.42	1.17	85.58	0.36	0.01133	0.00005	0.81602	0.14040	0.00357	0.00378	1.79E−12	7.56E−15	98.7
Mica 1-4	1869.8	11.7	86.07	0.75	86.13	0.29	0.02104	0.00234	1.20602	0.14033	0.00000	0.00000	1.45E−12	4.78E−15	100.0
Mica 1-5	1838.7	18.8	83.78	1.30	84.97	0.71	0.00744	0.00372	1.67297	0.18641	0.00329	0.00372	9.08E−13	7.56E−15	98.7
Mica 3-5	1796.5	14.1	80.75	0.92	82.39	0.49	0.00794	0.00265	1.36766	0.15928	0.00495	0.00265	1.28E−12	7.56E−15	98.1
CS0394 white mica; in situ[b]															
Mica 3-1	1750.8	7.5	76.07	0.34	77.35316	0.34	0.01091	0.00089	0.30806	0.00137	0.00435	0.00002	3.06E−12	1.36E−14	98.3
Mica 3-2	1763.4	6.9	76.93	0.27	76.89092	0.27	0.01092	0.00004	0.46235	0.00164	0.00000	0.00000	1.53E−12	5.42E−15	100.0
Mica 3-3	1763.4	6.7	76.92	0.25	78.45269	0.26	0.01247	0.00135	0.88124	0.05806	0.00518	0.00002	1.00E−12	3.03E−15	98.0
Mica 2-1	1794.9	6.8	79.10	0.25	79.50254	0.25	0.01179	0.00077	0.63331	0.07361	0.00137	0.00000	1.77E−12	5.59E−15	99.5
Mica 2-2	1763.9	5.9	76.96	0.13	77.35447	0.13	0.01293	0.00140	0.24392	0.06020	0.00134	0.00000	1.93E−12	3.03E−15	99.5
Mica 2-3	1752.1	6.0	76.15	0.14	76.58173	0.14	0.01064	0.00148	0.12913	0.06374	0.00145	0.00000	1.83E−12	3.03E−15	99.4
Mica 3-4	1768.3	6.4	77.26	0.20	77.61491	0.21	0.01210	0.00131	0.45698	0.11280	0.00119	0.00000	2.07E−12	5.42E−15	99.5
Mica 3-5	1751.6	5.7	76.12	0.05	76.93872	0.05	0.01194	0.00291	0.50769	0.25061	0.00278	0.00000	9.31E−13	0.00E+00	98.9
Mica 2-5	1754.6	6.2	76.33	0.18	77.66438	0.18	0.01933	0.00005	0.71960	0.10151	0.00453	0.00001	1.15E−12	2.71E−15	98.3
Mica 2-6	1819.9	6.8	80.85	0.25	80.80014	0.25	0.01247	0.00004	0.66335	0.00202	0.00000	0.00000	8.92E−13	2.71E−15	100.1
CS0377 white mica; in situ[c]															
Mica 2-3-1	1707.0	6.2	73.13	0.19	74.52	0.19	0.01247	0.00003	0.54928	0.15339	0.00472	0.00001	1.11E−12	2.71E−15	98.1
Mica 1-1	1738.3	5.9	75.23	0.12	75.22	0.12	0.01128	0.00002	0.14197	0.07008	0.00000	0.00000	1.73E−12	2.71E−15	100.0
Mica 3-1	1719.1	11.0	73.93	0.63	73.93	0.19	0.01367	0.00103	0.00000	0.00000	0.00000	0.00000	1.32E−12	3.03E−15	100.0
Mica 3-2	1749.4	6.9	75.97	0.27	75.97	0.13	0.01183	0.00040	0.07197	0.00012	0.00000	0.00000	3.41E−12	5.59E−15	100.0
Mica 3-2-2	1747.2	5.9	75.82	0.13	75.81	0.13	0.01438	0.00074	0.20042	0.06596	0.00000	0.00000	1.84E−12	3.03E−15	100.0
Mica 3-3	1739.8	5.8	75.32	0.11	75.32	0.11	0.01010	0.00066	0.05944	0.05869	0.00000	0.00000	2.06E−12	3.03E−15	100.0
Mica 3-5	1732.0	6.5	74.80	0.22	74.80	0.16	0.01165	0.00103	0.00000	0.00000	0.00000	0.00000	2.62E−12	5.59E−15	100.0
Mica 3-6	1752.7	6.2	76.20	0.18	76.65	0.09	0.01480	0.00103	0.02335	0.06917	0.00154	0.00052	2.63E−12	3.03E−15	99.4
Mica 3-7	1721.1	5.8	74.07	0.11	74.07	0.11	0.01450	0.00129	0.00000	0.00000	0.00000	0.00000	2.11E−12	2.71E−15	100.0
Mica 1-2	1735.2	6.2	75.01	0.18	75.01	0.18	0.01688	0.00206	0.00000	0.00000	0.00000	0.00000	1.32E−12	2.71E−15	100.0
Mica 2-3-2	1755.2	6.5	76.37	0.23	76.37	0.23	0.01197	0.00003	0.00000	0.00000	0.00000	0.00000	9.29E−13	2.71E−15	100.0
Mica 3-9	1718.9	6.8	73.92	0.26	73.92	0.26	0.01619	0.00006	0.00000	0.00000	0.00000	0.00000	1.55E−12	5.42E−15	100.0
CS0392 white mica[d]															
Mica 1-1	1761.1	7.6	76.63	0.35	76.60	0.25	0.00976	0.00003	0.38680	0.07638	0.00000	0.00000	1.71E−12	5.59E−15	100.0
Mica 1-2	1779.1	7.8	77.86	0.37	77.86	0.19	0.01528	0.00004	0.00000	0.00000	0.00000	0.00000	1.27E−12	3.03E−15	100.0
Mica 1-3	1741.7	7.9	75.31	0.38	75.29	0.27	0.01285	0.00005	0.26229	0.19301	0.00000	0.00000	1.51E−12	5.42E−15	100.0
Mica 1-4-2	1780.4	7.4	77.95	0.32	84.98	0.32	0.01343	0.00005	0.22845	0.04512	0.02378	0.00048	2.90E−12	1.08E−14	91.7
Mica 2-1	1809.5	6.9	79.97	0.26	80.64	0.23	0.01333	0.00004	0.22696	0.04482	0.00226	0.00046	2.92E−12	8.24E−15	99.2
Mica 2-2	1784.4	6.2	78.22	0.18	78.80	0.13	0.01332	0.00002	0.27794	0.03920	0.00196	0.00041	3.34E−12	5.59E−15	99.3
Mica 2-3	1779.8	6.5	77.91	0.22	78.32	0.16	0.01248	0.00003	0.44666	0.04900	0.00141	0.00051	2.67E−12	5.42E−15	99.5
Mica 2-4	1809.8	6.2	79.99	0.17	80.11	0.08	0.01147	0.00001	0.34860	0.04917	0.00042	0.00051	2.67E−12	2.71E−15	99.8
Mica 2-5	1768.5	8.0	77.13	0.38	77.26	0.33	0.01171	0.00067	0.92176	0.00392	0.00044	0.00067	2.02E−12	8.57E−15	99.8
Mica 2-6	1777.8	6.6	77.77	0.24	78.36	0.21	0.01153	0.00042	0.40801	0.00107	0.00198	0.00042	3.26E−12	8.57E−15	99.3
Mica 1-5	1764.3	8.3	76.85	0.42	77.03	0.36	0.00970	0.00073	0.42813	0.00197	0.00062	0.00073	1.86E−12	8.57E−15	99.8
Mica 1-6	1808.5	6.2	79.90	0.18	95.64	0.13	0.02342	0.00047	1.18877	0.09029	0.05328	0.00047	2.91E−12	3.83E−15	83.5

Table 3 (*Continued*)

Analysis	Age (Ma)	±	$^{40}Ar^*/^{39}Ar$	±	$^{40}Ar/^{39}Ar$	±	$^{38}Ar/^{39}Ar$	±	$^{37}Ar/^{39}Ar$	±	$^{36}Ar/^{39}Ar$	±	^{39}Ar (cm^3)	±	% $^{40}Ar^*$
CS0371 white mica[e]															
Grain 1: c 1	1886.2	8.1	85.45	0.41	87.33	0.32	0.01585	0.00006	0.06241	0.03081	0.00635	0.00091	2.98E−12	3.45E−14	97.9
Grain 1: r2	1816.6	6.9	80.46	0.27	81.49	0.07	0.01434	0.00001	0.08999	0.02961	0.00347	0.00087	3.10E−12	3.56E−14	98.7
Grain 1: r3	1781.1	7.0	77.99	0.28	78.17	0.21	0.01183	0.00003	0.12104	0.03259	0.00061	0.00064	2.12E−12	1.74E−14	99.8
Grain 1:c4	1770.6	8.0	77.27	0.39	77.27	0.33	0.01439	0.00006	0.10845	0.03569	0.00000	0.00000	1.93E−12	1.61E−14	100.0
Grain 1: c5	2018.6	7.1	95.48	0.29	96.65	0.17	0.00985	0.00002	0.23396	0.03038	0.00394	0.00080	1.69E−12	1.10E−14	98.8
Grain 1: c6	2043.4	7.5	97.45	0.34	97.45	0.28	0.01122	0.00003	0.12929	0.01161	0.00000	0.00000	1.98E−12	1.55E−14	100.0
Grain 1: c7	2158.2	7.3	106.89	0.31	110.16	0.22	0.01214	0.00002	0.19092	0.01257	0.01104	0.00074	1.83E−12	1.27E−14	97.0
Grain 2: c8	1818.6	8.5	80.60	0.44	100.13	0.13	0.02107	0.00003	0.14367	0.01091	0.06608	0.00144	2.11E−12	1.67E−14	80.5
Grain 2: 9	1800.9	9.5	79.37	0.53	79.37	0.50	0.01409	0.00009	0.03231	0.03189	0.00000	0.00000	2.17E−12	2.20E−14	100.0
Grain 1: 10	1849.6	6.7	82.80	0.24	99.99	0.14	0.02588	0.00004	0.03627	0.03581	0.05815	0.00071	1.93E−12	1.41E−14	82.8
CS 364 biotite and white mica; in situ[f]															
Mica 1	1780.8	5.9	78.12	0.12	78.33	0.12	0.01230	0.00002	0.07721	0.01759	0.00069	0.00000	3.84E−12	5.47E−14	99.7
Mica 2	1751.9	5.8	76.14	0.10	76.43	0.10	0.01262	0.00001	0.14670	0.02556	0.00099	0.00000	2.64E−12	2.60E−14	99.6
Mica 3	1754.9	9.9	76.35	0.55	76.35	0.15	0.01044	0.00001	0.07507	0.01059	0.00000	0.00000	2.13E−12	1.70E−14	100.0
Mica 4	1771.7	7.1	77.50	0.29	77.50	0.09	0.01442	0.00002	0.10267	0.01744	0.00000	0.00000	2.89E−12	3.10E−14	100.0
Mica 5	1753.2	6.8	76.23	0.26	76.23	0.19	0.01450	0.00004	0.05960	0.00014	0.00000	0.00000	2.30E−12	2.03E−14	100.0
Mica 6	1754.7	7.8	76.33	0.37	76.33	0.18	0.01094	0.00003	0.28793	0.00069	0.00000	0.00000	1.27E−12	6.68E−15	100.0
Mica 7	1742.1	6.3	75.48	0.19	76.22	0.20	0.01243	0.00064	0.17228	0.02127	0.00251	0.00001	2.12E−12	1.75E−14	99.0
Mica 8	1764.9	5.8	77.03	0.10	77.79	0.10	0.01405	0.00065	0.19835	0.02176	0.00256	0.00000	2.08E−12	1.61E−14	99.0
Mica 9	1750.4	9.4	76.04	0.51	77.70	0.39	0.01272	0.00113	0.11433	0.00058	0.00561	0.00113	1.20E−12	8.07E−15	97.9
Mica 10	1753.2	9.4	76.23	0.52	77.23	0.40	0.01051	0.00114	0.11548	0.00059	0.00338	0.00114	1.19E−12	8.01E−15	98.7
Mica 11	1779.8	9.7	78.06	0.54	79.36	0.33	0.01963	0.00147	0.04983	0.00021	0.00440	0.00147	9.20E−13	4.95E−15	98.4
JAW 03-03 white mica[g]															
Spot 1	1172.3	5.7	42.39	0.18	42.70	0.08	0.01265	0.00002	0.28677	0.02178	0.00105	0.00056	4.83E−12	8.24E−15	99.3
Spot 2	1216.4	5.8	44.58	0.19	44.73	0.10	0.01210	0.00054	0.14766	0.02083	0.00050	0.00054	5.06E−12	1.09E−14	99.7
Spot 3	1197.5	4.9	43.63	0.11	43.70	0.06	0.01158	0.00059	0.24579	0.03467	0.00023	0.00030	4.56E−12	6.06E−15	99.8
Spot 4	1246.9	5.0	46.13	0.11	46.12	0.06	0.01350	0.00002	0.15323	0.03491	0.00000	0.00000	4.53E−12	6.06E−15	100.0
Spot 5	1248.4	6.4	46.21	0.23	46.57	0.13	0.01266	0.00003	0.28175	0.02530	0.00123	0.00065	4.17E−12	1.12E−14	99.2
Spot 6	1258.6	6.1	46.73	0.21	46.71	0.07	0.01292	0.00002	0.20906	0.02580	0.00000	0.00000	4.09E−12	6.06E−15	100.0
Spot 7	1213.3	6.9	44.42	0.26	44.42	0.05	0.01077	0.00001	0.05753	0.01136	0.00000	0.00000	4.65E−12	5.42E−15	100.0
Spot 8	1184.8	7.6	43.00	0.31	43.29	0.06	0.01337	0.00002	0.23011	0.02988	0.00097	0.00103	3.95E−12	5.42E−15	99.3
Spot 9	1211.2	5.1	44.32	0.13	44.40	0.09	0.01331	0.00003	0.10985	0.01205	0.00028	0.00031	4.39E−12	8.57E−15	99.8
Spot 10	1214.5	5.5	44.49	0.17	44.48	0.13	0.01017	0.00003	0.09798	0.03090	0.00000	0.00000	3.83E−12	1.12E−14	100.0
Spot 11	1179.7	4.9	42.75	0.11	42.73	0.06	0.01195	0.00032	0.21165	0.02749	0.00000	0.00000	4.30E−12	6.06E−15	100.0
Spot 12	1233.9	4.9	45.47	0.10	45.55	0.04	0.01359	0.00032	0.08945	0.02821	0.00030	0.00032	4.19E−12	3.83E−15	99.8
CS0350 white mica; in situ[h]															
Mica 1-1	1377.4	5.2	53.17	0.11	53.39	0.08	0.01262	0.00002	0.22513	0.05849	0.00074	0.00027	5.07E−12	6.06E−15	99.6
Mica 1-2	1403.4	5.4	54.62	0.13	54.62	0.10	0.01278	0.00054	0.06002	0.05926	0.00000	0.00000	5.00E−12	8.57E−15	100.0
Mica 2-1c	1645.6	5.9	69.14	0.15	69.50	0.15	0.01224	0.00032	0.21457	0.01413	0.00124	0.00000	4.20E−12	8.68E−15	99.5
Mica 2-2	1332.8	5.2	50.74	0.11	51.10	0.11	0.01236	0.00031	0.12333	0.01353	0.00120	0.00000	4.39E−12	8.68E−15	99.3
Mica 2-3	1417.1	5.7	55.39	0.17	55.91	0.13	0.00972	0.00002	0.21031	0.04792	0.00177	0.00036	3.72E−12	7.67E−15	99.1
Mica 3-1c	1528.6	7.5	61.88	0.32	62.45	0.26	0.01115	0.00004	0.51269	0.08934	0.00191	0.00068	2.00E−12	7.67E−15	99.1
Mica 3-1r	1429.1	5.2	56.07	0.09	57.20	0.09	0.01198	0.00130	0.23065	0.05693	0.00383	0.00000	2.09E−12	2.71E−15	98.0
Mica 3-2	1172.7	4.4	42.49	0.05	42.71	0.05	0.01309	0.00080	0.17729	0.03501	0.00075	0.00000	3.40E−12	2.71E−15	99.5

Table 3 (*Continued*)

Mica 3-3	1371.1	6.6	52.83	0.25	53.28	0.20	0.01236	0.00053	0.18640	0.00062	0.00152	0.00052	2.59E−12	8.57E−15	99.2
Mica 2-1r	1328.5	5.9	50.51	0.19	51.25	0.11	0.01199	0.00051	0.13570	0.00020	0.00251	0.00051	2.67E−12	3.83E−15	98.6
Mica 1-3	1326.3	5.1	50.39	0.10	50.38	0.10	0.01293	0.00003	0.18706	0.03078	0.00000	0.00000	3.87E−12	7.67E−15	100.0
Mica 1-1-2	1464.8	5.3	58.12	0.11	58.34	0.11	0.01247	0.00002	0.21657	0.03564	0.00076	0.00000	3.34E−12	6.06E−15	99.6
CS0399 white mica[i]															
Grain 1-1	1736.0	5.8	74.91	0.11	75.66	0.11	0.01306	0.00002	0.07658	0.07561	0.00253	0.00000	2.13E−12	3.03E−15	99.0
Grain 1-2	1754.0	6.0	76.13	0.14	76.47	0.14	0.01463	0.00003	0.17883	0.03531	0.00114	0.00000	4.56E−12	8.24E−15	99.6
Grain 1-3	1728.9	7.3	74.44	0.32	75.82	0.32	0.00960	0.00004	0.00000	0.00000	0.00468	0.00002	1.16E−12	4.89E−15	98.2
Grain 1-4	1761.4	6.2	76.63	0.18	77.43	0.18	0.01183	0.00003	0.00000	0.00000	0.00271	0.00001	4.00E−12	9.09E−15	99.0
Grain 1-5	1753.3	19.1	76.08	1.24	76.06	0.24	0.01405	0.00004	0.27528	0.16307	0.00000	0.00000	9.89E−13	3.03E−15	100.0
Grain 2-1	1769.0	13.6	77.15	0.85	77.41	0.29	0.00739	0.00003	0.10865	0.10726	0.00087	0.00270	1.50E−12	5.59E−15	99.7
Grain 2-2	1778.5	10.2	77.80	0.59	78.08	0.17	0.01468	0.00003	0.05761	0.01896	0.00094	0.00191	2.84E−12	6.06E−15	99.6
Grain 2-3	1754.7	6.7	76.18	0.24	76.17	0.10	0.01263	0.00002	0.14269	0.01658	0.00000	0.00000	7.26E−12	9.77E−15	100.0
Grain 2-4	1758.4	6.2	76.43	0.18	76.65	0.17	0.01369	0.00026	0.11595	0.01041	0.00076	0.00026	5.18E−12	1.12E−14	99.7
Grain 2-5	1749.9	6.0	75.85	0.14	76.66	0.09	0.01410	0.00039	0.11078	0.03494	0.00272	0.00039	3.45E−12	3.83E−15	99.0
Grain 2-6	1748.3	6.1	75.74	0.16	76.07	0.12	0.01198	0.00038	0.03038	0.02999	0.00112	0.00038	3.60E−12	5.42E−15	99.6
Grain 2-7	1760.5	6.1	76.57	0.16	77.12	0.12	0.01413	0.00037	0.00000	0.00000	0.00186	0.00037	3.64E−12	5.42E−15	99.3
CS0341 white mica; in situ[j]															
Mica 1-1	1713.2	12.4	73.54	0.74	73.54	0.36	0.01223	0.00325	0.00000	0.00000	0.00000	0.00000	1.25E−12	6.06E−15	100.0
Mica 2-4	1792.4	10.0	78.92	0.57	78.91	0.30	0.00938	0.00249	0.10623	0.03496	0.00000	0.00000	1.63E−12	6.06E−15	100.0
Mica 2-4-2	1788.8	5.7	78.67	0.02	79.18	0.02	0.00716	0.00174	0.07435	0.00000	0.00173	0.00000	1.55E−12	0.00E+00	99.4
Mica 2-4-3	1731.9	6.2	74.79	0.18	75.50	0.18	0.01234	0.00003	0.00000	0.00000	0.00241	0.00001	1.13E−12	2.71E−15	99.1
Mica 2-2	1788.9	6.7	78.68	0.25	78.68	0.25	0.01266	0.00004	0.00000	0.00000	0.00000	0.00000	1.76E−12	5.42E−15	100.0
Mica 2-5	1771.5	5.7	77.48	0.06	77.48	0.06	0.01431	0.00000	0.00000	0.00000	0.00000	0.00000	1.36E−12	0.00E+00	100.0
Mica 2-6	1766.2	6.9	77.11	0.28	77.10	0.28	0.01278	0.00005	0.15210	0.00054	0.00000	0.00000	1.52E−12	5.42E−15	100.0
Mica 2-7	1779.3	7.1	78.01	0.29	78.01	0.29	0.00900	0.00003	0.10719	0.00040	0.00000	0.00000	2.16E−12	8.13E−15	100.0
Mica 2-8	1770.5	6.9	77.41	0.27	78.48	0.27	0.01460	0.00095	0.64960	0.08020	0.00363	0.00001	1.43E−12	4.89E−15	98.6
Mica 2-9	1756.5	7.2	76.45	0.31	77.05	0.31	0.01242	0.00110	0.65963	0.09307	0.00203	0.00001	1.23E−12	4.89E−15	99.2

[a] 1σ errors; J value = 0.021137 ± 0.000106; irradiation standard used = Tinto B biotite (409.24 ± 0.71 Ma).
[b] 1σ errors; J value = 0.021549 ± 0.000108; irradiation standard used = Tinto B biotite (409.24 ± 0.71 Ma).
[c] 1σ errors; J value = 0.021548 ± 0.000108; irradiation standard used = Tinto B biotite (409.24 ± 0.71 Ma).
[d] 1σ errors; J value = 0.021589 ± 0.000108; irradiation standard used = Tinto B biotite (409.24 ± 0.71 Ma).
[e] 1σ errors; J value = 0.021590 ± 0.000108; irradiation standard used = Tinto B biotite (409.24 ± 0.71 Ma).
[f] 1σ errors; J value = 0.021548 ± 0.000108; irradiation standard used = Tinto B biotite (409.24 ± 0.71 Ma).
[g] 1σ errors; J value = 0.021591 ± 0.000108; irradiation standard used = Tinto B biotite (409.24 ± 0.71 Ma).
[h] 1σ errors; J value = 0.021547 ± 0.000108; irradiation standard used = Tinto B biotite (409.24 ± 0.71 Ma).
[i] 1σ errors; J value = 0.021593 ± 0.000108; irradiation standard used = Tinto B biotite (409.24 ± 0.71 Ma).
[j] 1σ errors; J value = 0.021550 ± 0.000108; irradiation standard used = Tinto B biotite (409.24 ± 0.71 Ma).

a Ca-bearing phase (Fig. 8). We calculated muscovite Ar closure temperatures of 350 °C and 420 °C for this sample, using the average grain diameters of 100 μm and 1 cm, respectively (see section 3.1), with cylindrical diffusion geometry, and estimated cooling rate of 10 °C/Ma, using the Ar diffusion parameters of Hames and Bowring (1994) and the closure temperature equation of Dodson (1973). The muscovite is interpreted to have cooled through the muscovite Ar closure temperature range of 350–420 °C by 1827.7 ± 5.8 Ma (95% confidence).

Two biotite grains from sheared granite sample CS0431 produced ages between 1869 and 1805 Ma (Fig. 9, Table 2). Grain 1 yielded a plateau age of 1817.8 ± 3.3 Ma (1σ, MSWD = 0.76) for steps 2–6, representing 79.1% of the ^{39}Ar gas released (Fig. 9a). The large uncertainty on step 6 is due to the small amount of ^{39}Ar gas released. The age spectrum for grain 2 defined a plateau age of 1814.3 ± 3.5 Ma (1σ, MSWD = 2.2) for steps 2–4, representing 92% of the ^{39}Ar released (Fig. 9b), which is within error of the plateau age from grain 1 (Fig. 9c). These 500 μm diameter biotite grains are interpreted to have cooled through the biotite Ar closure temperature of 330 ± 50 °C by 1817.8–1814.3 Ma. The biotite Ar closure temperature was calculated for a 500 μm diameter grain, an estimated cooling rate of 10 °C/Ma, using cylindrical diffusion geometry, the Ar diffusion parameters of Grove and Harrison (1996), and the closure temperature equation of Dodson (1973).

3.2.2. $^{40}Ar/^{39}Ar$ UV laser spot analysis samples

The majority of samples dated yielded low ^{37}Ar/^{39}Ar ratios, and high %^{40}Ar* contents, suggesting negligible effects from Ca-bearing phases, and low atmospheric argon contents. These ratios are only discussed for samples that showed some possible effects due to the above.

White mica ^{40}Ar/^{39}Ar dated via the *in situ* UV laser technique in quartz-mica schist sample CS0395 produced a wide spread of ages, from 1870 to 1691 Ma. However, there is a broad cluster of ages between 1870 and 1760 Ma (Fig. 10a) and, excluding the youngest age of 1691 Ma that appears to be an outlier, a weighted mean was calculated from the oldest eight analyses and yielded an age of 1827 ± 32 Ma (95% confidence, MSWD = 4.8) (Fig. 10a, Table 3). The uncertainties on the analyses are relatively large owing to small amounts of gas released from the small white mica grains defining the foliation (Fig. 6f). To obtain more gas, a larger than normal (c. 200 μm) UV laser spot size was used, and for most analyses the beam was rastered over an area of c. 300–400 μm along the mica-bearing foliation. This may have resulted in the ablation of other minor K-bearing phases in the rock, thereby giving mixed ages. The relatively high $^{37}Ar_{Ca}/^{39}Ar_K$ ratios (Table 3) of some of the spot analyses indicate that some Ca-bearing phases were sampled during the UV laser ablation.

Biotite from quartz-mica schist sample CS0394 was ^{40}Ar/^{39}Ar dated via the *in situ* UV laser technique and produced a cluster of eight ages between 1768 and 1751 Ma, which yielded a weighted mean age of 1758.4 ± 4.4 Ma (95% confidence, MSWD = 1.18) (Fig. 10b, Table 3). Two older ages of 1819.9 ± 6.8 and 1794.9 ± 6.8 Ma (1σ) fall outside this group and were not included in the calculation of the weighted mean age. Due to the small grain sizes in this sample, two adjacent 90 μm laser spots were ablated for each analysis to obtain sufficient gas (Fig. 6e), which may have resulted in some of the observed age variation.

White mica from quartz–mica schist sample CS0377 was ^{40}Ar/^{39}Ar dated via the *in situ* UV laser technique and gave a spread of ages between 1755 and 1706 Ma (Fig. 10c, Table 3), yielding a weighted mean age of 1735.5 ± 9.6 Ma (95% confidence, MSWD = 5.6). Due to small grain sizes two adjacent 80–120 μm UV laser spots were ablated for each analysis to obtain sufficient gas.

Two grains of white mica from sheared pegmatite sample CS0392 were ^{40}Ar/^{39}Ar dated via the UV laser spot technique. The grains were c. 3.5 mm in diameter, and UV laser spot sizes of 70–120 μm were used. The ages fall into two groups: an older group of three analyses with ages of 1809.8 ± 6.2, 1809.5 ± 6.9, and 1808.5 ± 6.2 Ma (1σ), and a younger group with a spread of ages between 1784 and 1761 Ma (Fig. 10d, Table 3). These give weighted mean ages of 1809.3 ± 7.3 and 1776 ± 7 Ma (95% confidence, MSWD = 0.01 and 1.3), respectively. A younger analysis that gave an age of 1741.7 ± 7.9 Ma (1σ) was not included and was considered an outlier. The distribution of ages in each grain showed no apparent core to rim relationships. The two age groups may reflect partial resetting of the mica grains during cooling and/or deformation.

Two grains of white mica from deformed pegmatite sample CS0371 were ^{40}Ar/^{39}Ar UV laser dated. The grains were c. 8 mm in diameter, and a UV laser spot size of 70 μm was used. Two analyses of grain 1 were analysed from the left and right apparent grain rims (r2 and r3; Fig. 10e) and gave ages of 1816.6 ± 6.9 and 1781.1 ± 7.0 Ma (1σ), respectively (Table 3). With the exception of analysis c4, older ages between 2158.2 ± 7.3 and 1886.2 ± 8.1 Ma (1σ) were obtained from the core of the grain. However, these ages increased from the centre towards the apparent right rim of the grain. One possible explanation is that grain 1 was not a complete grain, i.e., it was a broken fragment, and the right rim is not actually a true rim, apart from where r3 was analysed yielding one of the youngest ages of 1781.1 ± 7.0 Ma (1σ) (Fig. 10e). However, the youngest age of 1770.6 ± 8.0 Ma (1σ) was analysed in the grain 'core', very close to the three oldest ages between 2058 and 2019 Ma (Fig. 10e), suggesting that the distribution of ages in this grain is complex. Two analyses from grain 2 gave ages of 1818.6 ± 8.5 and 1800.9 ± 9.5 Ma (1σ) (Table 3). Plotted together the two grains give a broad group of ages between 1886 and 1771 Ma, which give a weighted mean age of 1818 ± 36 Ma (95% confidence, MSWD = 27) (Fig. 10f). The older 'core' ages may reflect older relict ages, whilst the younger ages may reflect partial resetting ages for this coarse-grained white mica. Alternatively, the older ages may be due to the presence of excess ^{40}Ar in the grains.

Biotite and white mica from quartz-biotite schist sample CS0364 were ^{40}Ar/^{39}Ar dated *in situ* via UV laser technique using a UV laser spot size of 70 μm. They gave a spread of ages between 1781 and 1742 Ma, which gives a weighted mean age of 1760.6 ± 8.9 Ma (95% confidence, MSWD = 3.5) (Fig. 10g, Table 3).

Quartz-mica schist sample JAW-03-03 was a rock chip consisting of fine-grained white mica. A UV laser spot size of 70–80 μm was used to analyse the micas. The analyses gave a spread of ages between 1259 and 1172 Ma (Fig. 10h, Table 3). These fall into three, evenly distributed groups with weighted mean ages of 1250.7 ± 6.5, 1213.7 ± 5.6, and 1178.1 ± 6.5 Ma (95% confidence, MSWD = 1.19, 0.16 and 0.96, respectively).

Muscovite from granitic gneiss sample CS0350 was $^{40}Ar/^{39}Ar$ UV laser dated *in situ* using a UV laser spot size of 80 μm. The analyses gave a broad spread of ages between 1646 and 1173 Ma (Fig. 10i, Table 3). Mica grain 2-1 had an older core age of 1645.6 ± 5.9 Ma (1σ), compared to 1328.5 ± 5.9 Ma (1σ) for its rim. Mica grain 3-1 also showed this relationship with a core age of 1528.6 ± 7.5 Ma (1σ), compared to 1429.1 ± 5.2 Ma (1σ) for its rim. The core-rim age relationship and the broad spread of ages suggest that the white mica $^{40}Ar/^{39}Ar$ ages were not fully reset during a subsequent thermal event(s).

Two grains of white mica from quartz-mica schist sample CS0399 were $^{40}Ar/^{39}Ar$ dated using a UV laser spot size of 70–90 μm. The analyses gave a spread of ages between 1778 and 1729 Ma (Fig. 10j, Table 3). This yielded a weighted mean age of 1752.2 ± 7.5 Ma (95% confidence, MSWD = 2.9). The two grains gave similar ages with weighted means of 1746 ± 17 Ma (95% confidence, MSWD = 4.1) for grain 1, and 1756.4 ± 7.9 Ma (95% confidence, MSWD = 1.5) for grain 2. The oldest age of 1778.5 ± 10.2 Ma (1σ) came from the centre of grain 2; otherwise there were no clear core to rim relationships.

White mica from quartz-mica schist sample CS0341 was $^{40}Ar/^{39}Ar$ dated *in situ* using a UV laser spot size of 70 to 90 μm. The results show a spread of ages between 1792 and 1713 Ma (Fig. 10k, Table 3). Excluding the two youngest ages of 1732 and 1713 Ma, the remaining 8 analyses yielded a weighted mean age of 1776 ± 10 Ma (95% confidence, MSWD = 3.2). Due to the small grain sizes two adjacent spots were ablated for each analysis to obtain sufficient gas. This, and the presence of both coarser-grained muscovite and finer-grained sericite (Fig. 6m) may account for some of the spread in the ages due to mixing of the two forms of white mica that may have either crystallised or recrystallised at different times, resulting in the preservation of different ages.

3.3. Interpretation of $^{40}Ar/^{39}Ar$ results

$^{40}Ar/^{39}Ar$ dating of hornblende, white mica and biotite has produced a range of predominantly Proterozoic ages. The range of $^{40}Ar/^{39}Ar$ ages in hornblende sample CS-491 is probably the result of a long and disturbed history, possibly commencing before 2961 Ma. If the apparent age of the highest-temperature step of 2961.4 ± 10.4 Ma (1σ) is not due to the effects of excess ^{40}Ar, then this age suggests that the protolith is at least this old. The sample is interpreted as a metamorphosed dyke that may have intruded its granitic host during formation of the granitic gneissic fabric, possibly during a metamorphic event at c. 3.3 Ga (Nutman et al., 1991; Pidgeon and Wilde, 1998). The older K–Ar age of 3248 ± 64 Ma (2σ, H. Zwingmann, written communication, 2004) for hornblende sample CS-491 is within error of this c. 3.3 Ga metamorphic event, and may reflect the maximum age of the hornblende. The spread of younger $^{40}Ar/^{39}Ar$ hornblende ages may reflect heterogeneous resetting of the Ar systematics. The hornblende low-temperature $^{40}Ar/^{39}Ar$ plateau age of 2041 ± 4 Ma (1σ) (Fig. 7) is slightly older than the Glenburgh Orogeny (2005–1960 Ma, Occhipinti

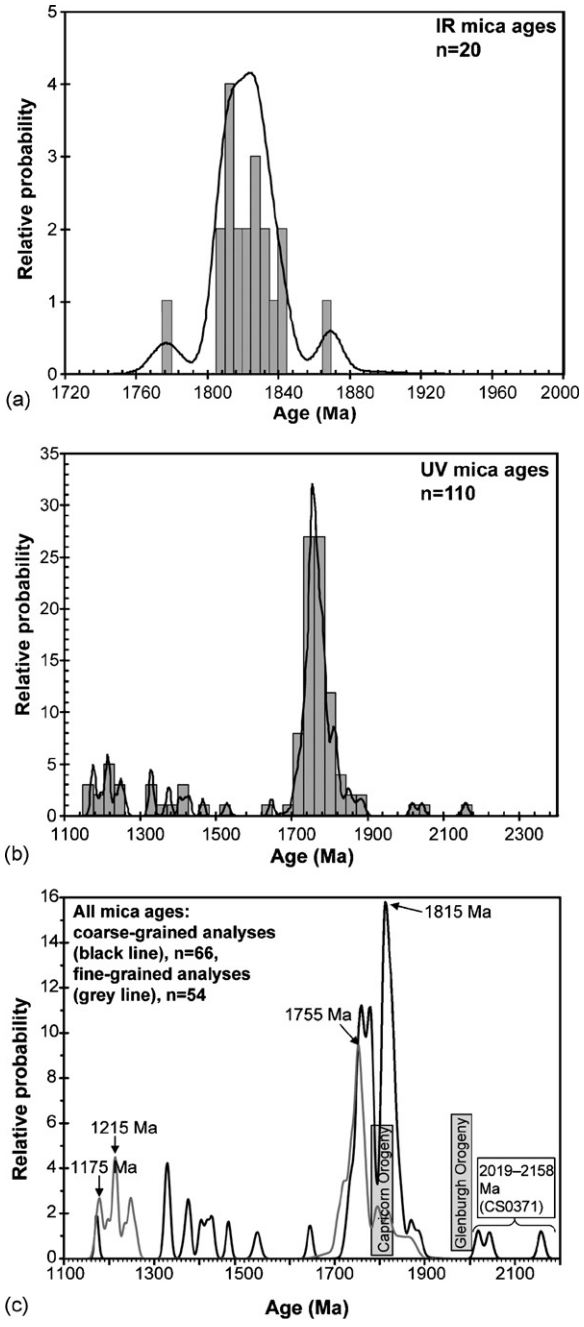

Fig. 11. (a) Probability density plot of all $^{40}Ar/^{39}Ar$ ages obtained from the IR laser step-heating white mica and biotite analyses. (b) Probability density plot of all $^{40}Ar/^{39}Ar$ ages obtained from UV laser white mica and biotite analyses. (c) Probability density plot of all $^{40}Ar/^{39}Ar$ ages from fine- (grey line) versus coarse-grained (black line) white mica and biotite to compare age differences. Fine-grained samples plotted are: CS0394, CS0395, CS0377, CS0364, JAW-03-03; $n = 54$. Coarse-grained samples plotted are: CS0350, CS0371, CS0392, CS0399, CS0416, CS0431; $n = 66$. The oldest ages are from one very coarse-grained sample, CS0371. Sample CS0341 was not included because it contains both coarse and fine micas that could not be differentiated during analysis. See text for additional explanation.

et al., 2004). The preservation of older high-temperature ages and a lower-temperature plateau age suggests that the Glenburgh orogenic event and associated thermal event may have resulted in partial $^{40}Ar^*$ loss in the hornblende. However, either the temperature of the thermal event was not high enough, (i.e., <510 °C (see Section 3.2.1), or the duration of the thermal pulse was too short to completely reset the age, resulting in the observed range of $^{40}Ar/^{39}Ar$ ages in this hornblende sample. In addition, deformation and metamorphism during the Capricorn Orogeny was predominantly under greenschist facies conditions in the southern part of the orogen (e.g., Occhipinti and Reddy, 2004), i.e., temperatures were not high enough to reset the $^{40}Ar/^{39}Ar$ ages in this hornblende sample. This is consistent with the greenschist overprint observed on most mafic schists in the belt (Wilde and Pidgeon, 1990; Spaggiari, 2007a). Deformed coarse-grained white mica pegmatite sample CS0371 also preserved some older white mica $^{40}Ar/^{39}Ar$ ages of 2158 ± 7, 2043 ± 7, and 2019 ± 7 Ma (1σ) that, if not due to excess ^{40}Ar, suggest it retained part of an earlier cooling history. Rb–Sr ages of 2203 and 2069 Ma have been recorded in coarse-grained biotite from Mt Narryer, and are similarly interpreted as retaining an earlier history (Libby et al., 1999).

The majority of white mica and biotite $^{40}Ar/^{39}Ar$ ages cluster between 1900 and 1700 Ma suggesting that the main phase of cooling through the white mica and biotite Ar closure temperatures (420–300 °C (Lister and Baldwin, 1996) and 300 ± 50 °C (Grove and Harrison, 1996), respectively) in the Jack Hills region was complete by c. 1700 Ma (Fig. 11). Cooling by c. 1700 Ma is interpreted to have followed the main phase of transpressive, dextral shearing along the Cargarah Shear Zone, as most foliations targeted were related to this. The spread in the $^{40}Ar/^{39}Ar$ ages is interpreted to be due to the long and complex deformation history of the belt, including variable movement and reactivation of the shear zone network over a substantial period of time. This has resulted in partial resetting of the $^{40}Ar/^{39}Ar$ ages during deformation and/or cooling, producing heterogeneous distributions of $^{40}Ar^*$ both within individual grains and also from sample to sample.

Two white mica samples (JAW-03-03 and CS0350) preserve younger $^{40}Ar/^{39}Ar$ deformation and/or cooling ages ranging from 1258.6 to 1172.3 Ma and 1645.6 to 1172.7 Ma, respectively, however, these events do not appear to have disturbed the Ar systematics in the other samples. These younger ages may reflect partial $^{40}Ar^*$ loss during a later event, possibly associated with the semi-brittle faulting that overprints the main foliation in the Jack Hills greenstone belt, such as the small fault zone from which JAW-03-03 was sampled. The youngest ages of 1172.7 ± 4.4 Ma (1σ) for sample CS0350 and 1172.3 ± 5.7 Ma (1σ) for sample JAW-03-03 are identical, and may indicate a maximum age for this younger resetting event. A weighted mean age of the 4 youngest ages from these two samples yielded an age of 1176.1 ± 5.2 Ma (1σ, MSWD = 0.96). It is interesting to note that these two samples are situated close together (c. 700 m across strike (Fig. 5g)) and may indicate a very localised deformation and/or cooling event of this age or younger.

The two mica samples dated by the $^{40}Ar/^{39}Ar$ IR laser step-heating method produced slightly older ages than the $^{40}Ar/^{39}Ar$ UV laser spot dated samples (Fig. 11a and b). Muscovite sample CS0416 yielded a complex age spectrum, with apparent ages ranging from 1841 to 1777 Ma (Fig. 8). IR laser step-heating of biotite grains from sample CS0431 yielded plateau ages of 1817.8 ± 3.3 and 1814.3 ± 3.5 Ma (1σ). These IR laser $^{40}Ar/^{39}Ar$ step-heating ages are mostly slightly older than, but not inconsistent with, the results from the UV laser $^{40}Ar/^{39}Ar$ dating method, which shows a large peak covering an area between c. 1800 and 1700 Ma (Fig. 11b). Given that only two mica samples were dated by the IR laser $^{40}Ar/^{39}Ar$ step-heating method, the difference between the ages may not be due to the different analytical techniques, but could either be due to grain size variations (i.e., larger grains retaining older ages) or could reflect that these samples have experienced different stages of movement within different parts of the shear zone network. $^{40}Ar/^{39}Ar$ UV laser spot analysis also allows specific regions within the mica grains to be dated and therefore picks up intra-grain heterogeneities more efficiently.

Several $^{40}Ar/^{39}Ar$ studies of deformed micas, particularly those using the UV laser spot technique, have shown that the formation of microstructures during deformation affects Ar retentivity, and that simple models of volume diffusive loss of Ar are not adequate (Hodges and Bowring, 1995; Reddy and Potts, 1999; Kramar et al., 2001). Development of microstructures typical to shear zones, such as shear bands and mica fish where the micas are effectively porphyroclasts, have been shown to produce apparent age groupings defining various deformation events, or mixed ages (Kramar et al., 2001; Mulch and Cosca, 2004). The partial recrystallisation of white micas during a deformation event can also produce different $^{40}Ar/^{39}Ar$ ages (Mulch and Cosca, 2004), and neocrystallisation can result in complete resetting of $^{40}Ar/^{39}Ar$ white mica ages due to the formation of new white mica grains during ductile deformation (Dunlap et al., 1991; Dunlap, 1997).

Variations in grain size are also a contributing factor to apparent age heterogeneity. Although the Ar diffusion rate is constant in white mica grains of all sizes, smaller grains will loose a greater percentage of their Ar during a short thermal event due to the shorter distances that the Ar must travel through the grain to 'escape' at the grain boundary/rim. In contrast, during the same short thermal event, the ^{40}Ar atoms must travel greater distances in large unfractured grains before they can 'escape', hence large white mica grains commonly preserve older ages in the grain cores. For example, if we take the approximate minimum and maximum white mica grain radii of 50 μm and 0.5 cm, respectively, and take a maximum greenschist facies metamorphic temperature of 500 °C (to roughly equate to the Capricorn Orogenic event), then a 0.5 cm white mica grain would require c. 6 Ma of heating to loose 50% of its $^{40}Ar^*$. However, at the same temperature of 500 °C, a 50 μm white mica grain would only need c. 630 years to loose 50% of its $^{40}Ar^*$, and the $^{40}Ar/^{39}Ar$ ages would be completely reset after c. 17,000 years at the same thermal event temperature. This Ar diffusion modelling assumed cylindrical diffusion geometry, which is appropriate for micas, and used the white mica Ar diffusion parameters of Hames and Bowring (1994).

This may be a partial explanation for the variation in ages in the mica samples dated in this study, as there appears to be some age versus grain size correlation (Fig. 11c). It can be seen from Fig. 11c that with the exception of white mica sample CS0350, the coarse grained micas all preserve older >1700 Ma $^{40}Ar/^{39}Ar$ ages, with the largest relative probability cluster at 1815 Ma, which coincides with the timing of the Capricorn Orogeny. In addition, they also produced the oldest recorded ages of 2158.2 Ma, 2043.4 and 2018.6 (Fig. 11c). In contrast, the fine grained micas yield younger, post-Capricorn Orogeny (1830–1780 Ma), $^{40}Ar/^{39}Ar$ ages, with the largest cluster at 1755 Ma, two smaller clusters at 1775 Ma and1215 Ma, and no ages of >1900 Ma preserved (Fig. 11c).

Deformation mechanisms that can affect grain sizes of micas are numerous, producing effects such as grain size reduction and overgrowths (Reddy and Potts, 1999). These studies show that dating deformation events, or the subsequent cooling from them, is complex, particularly in multiply-deformed rocks. Although a comprehensive microstructural study has not been undertaken on the samples dated in this study, the structural analysis of the belt shows that it is complex (Spaggiari, 2007b), and the Ar systematics would clearly have been affected by deformation. Therefore, although the data are still informative, some dispersion in the results is not surprising.

The presence of excess ^{40}Ar in a sample results in older $^{40}Ar/^{39}Ar$ and K–Ar apparent ages (e.g., Kelley, 2002). Excess ^{40}Ar, if present, may be derived from metamorphic fluids produced during degassing of nearby older minerals that contain a high $^{40}Ar^*$ component (e.g., Reddy et al., 1997). A possible source could be the Archean granitic rocks and gneisses surrounding the belt, and in fact, excess ^{40}Ar has been documented in shear zones within ancient metamorphic terrains (e.g., Allen and Stubbs, 1982; Smith et al., 1994; Vance et al., 1998). The very small amounts of atmospheric Ar in the samples means that inverse isochron plots, which can provide a method to check for the presence of excess ^{40}Ar (Roddick, 1978), cannot be defined. Hence, any possible effects of excess ^{40}Ar cannot be assessed. However, the presence of older core and younger rim ages in two coarse-grained white mica samples (CS0371 and CS0350) would argue against the presence of excess ^{40}Ar, as age profiles with older rim and younger core ages would be preserved if excess ^{40}Ar had partially entered these grains (e.g., Pickles et al., 1997).

In summary, the $^{40}Ar/^{39}Ar$ data are interpreted to reflect the complex deformation and/or cooling history shown by the structural data; in particular, variable shear zone movement during the Capricorn Orogeny. This is consistent with the known regional deformation history. Dextral transpression at greenschist facies conditions occurred during the Capricorn Orogeny within the Errabiddy Shear Zone, which marks the boundary between the Yilgarn Craton and the Glenburgh Terrane (Fig. 1; Occhipinti and Reddy, 2004). The Yarlarweelor Gneiss Complex (Fig. 1) also underwent dextral strike slip deformation during the Capricorn Orogeny (Sheppard et al., 2003). The $^{40}Ar/^{39}Ar$ mica data do not preserve any evidence of Late Archean deformation and metamorphism (Myers, 1990a,b), which involved intrusion of Neoarchean granites. This suggests most grains were either probably completely reset at a later stage, or that the micas dated mostly grew after c. 2600 Ma. The only samples to indicate some possible effects of the 2005–1960 Ma Glenburgh Orogeny in the Jack Hills area are hornblende sample CS-491 and the large white mica grains from deformed pegmatite sample CS0371. Whether this marked an earlier phase of deformation and cooling, possibly even the initiation of the Cargarah Shear Zone, is unknown.

4. Discussion and conclusions

The $^{40}Ar/^{39}Ar$ dating presented here shows that the majority of samples from the southeastern part of the Narryer Terrane were deformed and cooled through the white mica Ar closure temperature during the Paleoproterozoic, by c. 1700 Ma. This deformation produced major east- to northeast-trending dextral shear zones and related structures that are interpreted to extend as far south as the northern part of the Mingah Range greenstone belt in the Murchison Domain, and include the Yalgar Fault (Figs. 1, 3 and 4). The deformation is interpreted to be primarily due to the Capricorn Orogeny, although as shown in this $^{40}Ar/^{39}Ar$ study, there may have been some localised younger deformation and/or cooling events. The timing of the Capricorn Orogeny (1830–1780 Ma) is based on the ages of granite intrusions, which have recorded the main thermal pulse associated with the orogeny (e.g., Sheppard et al., 2003). Many of the $^{40}Ar/^{39}Ar$ white mica and biotite ages, particularly from the fine-grained samples, show a cluster of ages at 1760–1740 Ma (Figs 10a, b, d, g, j, k, and 11), after the main thermal pulse of the Capricorn Orogeny. This may indicate a localised post-Capricorn event. Alternatively, it may indicate that deformation and/or cooling was ongoing in the southeastern Narryer Terrane, following the main orogenic thermal pulse. Given the intracratonic setting (e.g., Sheppard, 2005) either explanation is reasonable as the deformation would have been driven by far-field stresses.

Apart from the Glenburgh Orogeny, the Proterozoic deformation events that have affected the northwestern part of the Yilgarn Craton have all taken place in an intracratonic setting (Sheppard, 2005; Sheppard et al., 2005). The Capricorn Orogeny is now interpreted as a widespread intracratonic event because of the absence of any subduction-related rocks, such as magmatic arc and sedimentary rocks that could be related to events leading to collision of the Pilbara and Yilgarn Cratons (Sheppard, 2005). That collision is now interpreted to have taken place during the Glenburgh Orogeny, with the Glenburgh Terrane possibly already accreted to the Pilbara Craton (Sheppard, 2005).

Intracratonic reworking within the Capricorn Orogen also took place during the 1680–1620 Ma Mangaroon Orogeny (Sheppard et al., 2005) but this does not appear to have affected the northwestern part of the Yilgarn Craton. The $^{40}Ar/^{39}Ar$ data suggest a possible younger event occurred at c. 1172 Ma. This younger deformation and/or cooling event may be related to widespread mafic dyke emplacement (part of the c. 1210 Ma Marnda Moorn large igneous province) that occurred in the northwestern part of the Yilgarn Craton (Wingate et al., 2005). The c. 1215 Ma group of $^{40}Ar/^{39}Ar$ ages (sample JAW-03-03) is

close to the intrusive age of an east-trending, leucogabbro dyke in the southwestern part of the Jack Hills greenstone belt, which has a SHRIMP U–Pb zircon age of 1211 ± 3 Ma (95% uncertainties, MSWD = 1.02), and is similar to a dyke that intruded into granite 30 km south of the belt that has a SHRIMP U–Pb age of c.1213 Ma (Wingate et al., 2005).

The confirmation of the presence of intracratonic, large-scale Proterozoic structures in the southeastern Narryer Terrane and northern Murchison Domain (Youanmi Terrane) has implications for understanding the nature of the tectonic boundary between the two terranes. This is presently defined as the Yalgar and Balbalinga Faults (Myers, 1993; Myers and Hocking, 1998). Terrane amalgamation predated Neoarchean granites, which are present within both terranes (Nutman et al., 1991, 1993; Myers, 1993), and has been interpreted as having formed a suture zone following subduction and collision (Myers, 1995). It is not clear whether this suturing took place along the Yalgar Fault, although it was suggested by Myers (1990b). If the Yalgar Fault was a zone of Archean suturing, followed by reactivation in the Proterozoic, and is still active, as has been suggested, then one would expect it to be well-defined in the geophysical datasets. However, its lack of definition in the east in the new gravity data is at odds with this interpretation (Fig. 4). In the aeromagnetic data it is defined as a discontinuous series of linked faults, similar to the east- to east-northeast-trending faults described above (Section 2.2), rather than as a major structural boundary. It is possible that the Yalgar Fault formed at the same time as the Cargarah Shear Zone, and that these east- to east-northeast-trending faults are effectively feather faults (or horse-tails), formed in response to movement along the craton margin during the Proterozoic (i.e., along the Errabiddy Shear Zone) (*cf.* Williams et al., 1983b; Williams, 1986; Myers, 1995).

More geochronological data are necessary to test whether the Narryer and Youanmi Terranes were truly exotic, or whether they share a common basement (e.g., Wyche et al., 2004). If terrane collision did occur, then the terrane boundary may be cryptic and difficult to locate structurally and lithologically due to reworking.

Acknowledgements

This work has been supported by Australian Research Council Grant DP0211706 (awarded to R.T. Pidgeon, S.A. Wilde, and A.A. Nemchin), the Tectonics Special Research Centre, and the Geological Survey of Western Australia. We thank Sandra Occhipinti for her comments and an anonymous reviewer for their intemperate review which prompted us to reassess the Yalgar Fault. A third anonymous reviewer is thanked for their comments. This paper is published with the permission of the director of the Geological Survey of Western Australia.

Appendix A. $^{40}Ar/^{39}Ar$ laser dating techniques

For the IR laser $^{40}Ar/^{39}Ar$ step-heating mineral grains were handpicked, cleaned in methanol, and rinsed in deionised water in an ultrasonic bath. For the *in situ* $^{40}Ar/^{39}Ar$ UV laser spot-analyses a polished thick section (100–200 μm thickness) was removed from its glass slide, and the sample rinsed ultrasonically in methanol and subsequently deionised water. 10 mm × 10 mm sections of interest were broken off the polished thick section. Samples were then individually wrapped in aluminium foil, and all the samples were loaded into an aluminium package. Biotite age standard Tinto B (K–Ar age of 409.24 Ma (Rex and Guise, 1995), was loaded at 5 mm intervals along the package to monitor the neutron flux gradient. The 13 $^{40}Ar/^{39}Ar$ samples were contained in 2 Cd-shielded packages (in 2003 and 2004) and irradiated in the 5C position of the McMaster University Nuclear Reactor, Hamilton, Canada, for 90 h (2003) and 89.1 h (2004). Samples CS0341, CS0350, CS0364, CS0371, CS0377, CS0392, CS0394 and CS0399 were irradiated in 2003, and samples CS0395, CS0416, CS0431 and CS-491 were irradiated in 2004. Upon return, the IR laser step-heating samples were loaded into an ultra-high vacuum laser chamber with a Kovar viewport. The UV laser spot analysis samples were loaded into an ultra-high vacuum laser chamber with a Suprasil 2 viewport. All samples were baked to 120 °C overnight to remove adsorbed atmospheric argon from the samples and chamber walls.

For the $^{40}Ar/^{39}Ar$ IR laser step-heating samples, a 110 W Spectron Laser Systems continuous-wave neodymium–yttrium–aluminium–garnet (CW-Nd-YAG) (λ = 1064 nm) laser, fitted with a TEM00 aperture, was used to slowly laser step-heat the mineral sample, at increasing laser powers from 10.0–10.2 A (CS-491), 9.9–10.1 A (CS0431), and 10.1–10.6 A (CS0416). For the $^{40}Ar/^{39}Ar$ UV laser spot analyses a New Wave Research LUV 213X 4 mJ pulsed quintupled Nd-YAG laser (λ = 213 nm), with a variable spot size of 10–350 μm, and a repetition rate of 10 Hz, was used to ablate the mineral grains. The lasers were fired through a Merchantek computer-controlled X–Y–Z sample chamber stage and microscope system, fitted with a high-resolution CCD camera, 6× computer controlled zoom, high magnification objective lens, and two light sources for sample illumination.

The gases released by laser heating/ablation were 'gettered' using 3 SAES AP10 getter pumps to remove all active gases. The remaining noble gases were equilibrated into a high sensitivity mass spectrometer (MAP 215-50), operated at a resolution of 600, and fitted with a Balzers SEV 217 multiplier. The automated extraction and data acquisition system was computer controlled, using a LabView program. For the $^{40}Ar/^{39}Ar$ IR laser step-heating samples the mean 4 min extraction system blank Ar isotope measurements obtained during the experiments were 1.51×10^{-12}, 1.30×10^{-14}, 2.25×10^{-15}, 3.94×10^{-14}, and 1.52×10^{-14}, cm^3 STP (standard temperature and pressure) for ^{40}Ar, ^{39}Ar, ^{38}Ar, ^{37}Ar, and ^{36}Ar respectively. For the $^{40}Ar/^{39}Ar$ UV laser spot-analyses the mean 3 or 4 min extraction system blank Ar isotope measurements obtained during the experiments were 1.61×10^{-11}, 9.78×10^{-14}, 2.31×10^{-13}, 4.14×10^{-13}, and 1.11×10^{-13}, cm^3 STP (standard temperature and pressure) for ^{40}Ar, ^{39}Ar, ^{38}Ar, ^{37}Ar, and ^{36}Ar respectively, for samples irradiated in 2003; and 3.82×10^{-12}, 1.49×10^{-14}, 5.41×10^{-15}, 5.95×10^{-14}, and 3.11×10^{-14} (4 min. blank), for sample CS0395, which was irradiated in 2004. Samples were corrected for mass spectrome-

ter discrimination ($^{40}Ar/^{36}Ar = 281.0$ (2003) and 283.4 (2004)) and nuclear interference reactions (($^{39}Ar/^{37}Ar)_{Ca}$ – 0.00065, $(^{36}Ar/^{37}Ar)_{Ca} = 0.000255$, and $(^{40}Ar/^{39}Ar)_{K} = 0.0015$). Errors quoted on the ages are 1σ, and the $^{40}Ar/^{39}Ar$ ages were calculated using the decay constant quoted by Steiger and Jäger (1977). *J* values and uncertainties are noted on the sample $^{40}Ar/^{39}Ar$ data tables (Tables 2 and 3). The $^{40}Ar/^{39}Ar$ data presented in this study were analysed at the Western Australian Argon Isotope Facility, within the John de Laeter Centre of Mass Spectrometry at Curtin University of Technology, operated by a consortium consisting of Curtin University of Technology and the University of Western Australia.

References

Allen, A.R., Stubbs, D., 1982. An $^{40}Ar/^{39}Ar$ study of a polymetamorphic complex in the Arunta Block, central Australia. Contrib. Mineral. Petrol. 79, 319–332.

Bodorkos, S., Wingate, M.T.D., in preparation. Compilation of geochronology data, 2008 update. Western Australia Geological Survey.

Cassidy, K.F., Champion, D.C., McNaughton, N.J., Fletcher, I.R., Whitaker, A., Bastrakova, I., Budd, A.R., 2002. Characterisation and metallogenic significance of Archaean granitoids of the Yilgarn Craton, Western Australia: Minerals and Energy Institute of Western Australia, Report 222, 538 pp.

Cassidy, K.F., Champion, D.C., Krapez, B., Barley, M.E., Brown, S.J.A., Blewett, R.S., Groenewald, P.B., Tyler, I.M., 2006. A revised geological framework for the Yilgarn Craton: Geological Survey of Western Australia, Record 2006/8.

Cavosie, A.J., Wilde, S.A., Liu, D., Weiblen, P.W., Valley, J.W., 2004. Internal zoning and U–Th–Pb chemistry of Jack Hills detrital zircons: a mineral record of early Archean to Mesoproterozoic (4348–1576 Ma) magmatism. Precamb. Res. 135, 251–279.

Cavosie, A.J., Valley, J.W., Wilde, S.A., E.I.M.F., 2005. Magmatic $\delta^{18}O$ in 4400–3900 Ma detrital zircons: a record of the alteration and recycling of crust in the Early Archean. Earth Planet. Sci. Lett. 235, 663–681.

Cawood, P.A., Tyler, I.M., 2004. Assembling and reactivating the Proterozoic Capricorn Orogen: lithotectonic elements, orogenies, and significance. Precamb. Res. 128, 201–218.

Compston, W., Pidgeon, R.T., 1986. Jack Hills, evidence of more very old detrital zircons in Western Australia. Nature 321, 766–769.

Dodson, M.H., 1973. Closure temperature in cooling geochronological and petrological systems. Contrib. Mineral. Petrol. 40, 259–274.

Dunlap, W.J., 1997. Neocrystallisation or cooling? $^{40}Ar/^{39}Ar$ ages of white micas from low-grade mylonites. Chem. Geol. 143, 181–203.

Dunlap, W.J., Teyssier, C., McDougall, I., Baldwin, S., 1991. Ages of deformation from K–Ar and $^{40}Ar/^{39}Ar$ dating of white micas. Geology 19, 1213–1216.

Dunn, S.J., Nemchin, A.A., Cawood, P.A., Pidgeon, R.T., 2005. Provenance record of the Jack Hills Metasedimentary Belt: source of the Earth's oldest zircons. Precamb. Res. 138, 235–254.

Elias, M., 1982. Belele, W.A. 1st ed.: Western Australia Geological Survey, 1:250 000 Geological Series Explanatory Notes, 22 pp.

Froude, D.O., Ireland, T.R., Kinny, P.D., Williams, I.S., Compston, W., Williams, I.R., Myers, J.S., 1983. Ion microprobe identification of 4100–4200 Myr-old terrestrial zircons. Nature 304, 616–618.

Geological Survey of Western Australia, 2006. Murchison geological exploration package (February 2006 update digital package). Geological Survey of Western Australia, Record 2006/2.

Grove, M., Harrison, T.M., 1996. $^{40}Ar^*$ diffusion in Fe-rich biotite. Am. Mineralogist 81, 940–951.

Hames, W.E., Bowring, S.A., 1994. An empirical evaluation of the argon diffusion geometry in muscovite. Earth Planet. Sci. Lett. 124, 161–169.

Harrison, T.M., 1981. Diffusion of ^{40}Ar in hornblende. Contrib. Mineral. Petrol. 78, 312–331.

Harrison, T.M., McDougall, I., 1980. Investigations of an intrusive contact, northwest Nelson, New Zealand. I. Thermal, chronological and isotopic constraints. Geochim. Cosmochim. Acta 44, 1985–2003.

Harrison, T.M., Blichert-Toft, J., Muller, W., Albarede, F., Holden, P., Mojzsis, S.J., 2005. Heterogeneous Hadean hafnium: evidence of continental crust at 4.4 to 4. 5 Ga. Science 310, 1947–1950.

Hodges, K.V., Bowring, S.A., 1995. $^{40}Ar/^{39}Ar$ thermochronology of isotopically zoned micas: insights from the southwestern USA Proterozoic orogen. Geochim. Cosmochim. Acta 59, 3205–3220.

Kelley, S., 2002. Excess argon in K–Ar and Ar–Ar geochronology. Chem. Geol. 188, 1–22.

Kent, A.J.R., McCuaig, T.C., 1997. Disturbed ^{40}Ar–^{39}Ar systematics in hydrothermal biotite and hornblende at the Scotia gold mine. Western Australia: evidence for argon loss associated with post-mineralisation fluid movement. Geochim. Cosmochim. Acta 61, 4655–4669.

Kinny, P.D., Nutman, A.P., 1996. Zirconology of the Meeberrie gneiss, Yilgarn Craton, Western Australia: an early Archaean migmatite. Precamb. Res. 78, 165–178.

Kinny, P.D., Williams, I.S., Froude, D.O., Ireland, T.R., Compston, W., 1988. Early Archaean zircon ages from orthogneisses and anorthosites at Mount Narryer, Western Australia. Precamb. Res. 38, 325–341.

Kinny, P.D., Wijbrans, J.R., Froude, D.O., Williams, I.S., Compston, W., 1990. Age constraints on the geological evolution of the Narryer Gneiss Complex, Western Australia. Aust. J. Earth Sci. 37, 51–69.

Kramar, N., Cosca, M.A., Hunziker, J.C., 2001. Heterogeneous $^{40}Ar^*$ distributions in naturally deformed muscovite: in situ UV laser ablation evidence for microstructurally controlled intragrain diffusion. Earth Planet. Sci. Lett. 192, 377–388.

Lee, J.K.W., 1993. The argon release mechanisms of hornblende *in vacuo*. Chem. Geol. 106, 133–170.

Lee, J.K.W., Onstott, T.C., Cashman, K.V., Cumbest, R.J., Johnson, D., 1991. A critical evaluation of the $^{40}Ar/^{39}Ar$ incremental heating of hornblende. Geology 19, 872–876.

Libby, W.G., De Laeter, J.R., Armstrong, R.A., 1999. Proterozoic biotite dates in the northwestern part of the Yilgarn Craton, Western Australia. Aust. J. Earth Sci. 46, 851–860.

Lister, G.S., Baldwin, S.L., 1996. Modeling the effect of arbitrary *P–T–t* histories on argon diffusion in minerals using the MacArgon program for the Apple Macintosh. Tectonophysics 253, 83–109.

Mojzsis, S.J., Harrison, T.M., Pidgeon, R.T., 2001. Oxygen-isotope evidence from ancient zircons for liquid water at the Earth's surface 4300 Ma ago. Nature 409, 178–181.

Mulch, A., Cosca, M.A., 2004. Recrystallisation or cooling ages: *in situ* UV-laser $^{40}Ar/^{39}Ar$ geochronology of muscovite in mylonitic rocks. J. Geol. Soc. Lond. 161, 573–582.

Myers, J.S., 1988. Early Archaean Narryer Gneiss Complex, Yilgarn Craton, Western Australia. Precamb. Res. 38, 297–307.

Myers, J.S., 1990a. Western Gneiss Terrane, in Geology and mineral resources of Western Australia. Western Aust. Geol. Survey Memoir 3, 13–31.

Myers, J.S., 1990b. Part 1 — summary of the Narryer Gneiss Complex. In: Ho, S.E., Glover, J.S., Myers, J.S., Muhling, J.R. (Eds.), Third International Archean Symposium. Perth, 1990, Excursion Guidebook, University of Western Australia, Geology Department and University Extension, Pub. 21, pp. 62–71.

Myers, J.S., 1993. Precambrian history of the West Australian Craton and adjacent orogens. Annu. Rev. Earth Planet. Sci. 21, 453–485.

Myers, J.S., 1995. The generation and assembly of an Archaean supercontinent: evidence from the Yilgarn Craton, Western Australia. In: Coward, M.P., Ries, A.C. (Eds.), Early Precambrian Processes. Geological Society Special Publication No. 95, pp. 143–154.

Myers, J.S., 1997. Byro, W.A. Sheet SG 50-10, second ed. Western Australia Geological Survey, 1:250 000 Geological Series.

Myers, J.S., Hocking, R.M., 1998. Geological map of Western Australia, 1:2,500,000, 13th ed. Western Australia Geological Survey.

Nemchin, A.A., Pidgeon, R.T., Whitehouse, M.J., 2006. Re-evaluation of the origin and evolution of >4.2 Ga zircons from the Jack Hills metasedimentary rocks. Earth Planet. Sci. Lett. 244, 218–233.

Nutman, A.P., Kinny, P.D., Compston, W., Williams, I.S., 1991. SHRIMP U–Pb zircon geochronology of the Narryer Gneiss Complex, Western Australia. Precamb. Res. 52, 275–300.

Nutman, A.P., Bennett, V.C., Kinny, P.D., Price, R., 1993. Large-scale crustal structure of the northwestern Yilgarn Craton, Western Australia: evidence form Nd isotopic data and zircon geochronology. Tectonics 12, 971–981.

Occhipinti, S.A., Reddy, S.M., 2004. Deformation in a complex crustal-scale shear zone: Errabiddy shear Zone, Western Australia. In: Alsop, G.I., Holdsworth, R.E., McCaffery, K.J.W., Hand, M. (Eds.), Flow Processes in Faults, Shear Zones, vol. 224. Geological Society of London, Special Publications, pp. 229–248.

Occhipinti, S.A., Sheppard, S., Myers, J.S., Tyler, I.M., Nelson, D.R., 2001. Archean and Paleoproterozoic geology of the Narryer Terrane (Yilgarn Craton) and the southern Gascoyne Complex (Capricorn Orogen), Western Australia — a field guide. Western Australia Geological Survey, Record 2001/8, 70 pp.

Occhipinti, S.A., Sheppard, S., Passchier, C., Tyler, I.M., Nelson, D.R., 2004. Palaeoproterozoic crustal accretion and collision in the southern Capricorn Orogen: the Glenburgh Orogeny. Precamb. Res. 128, 237–255.

Peck, W.H., Valley, J.W., Wilde, S.A., Graham, C.M., 2001. Oxygen isotope ratios and rare earth elements in 3.3 to 4. 4 Ga zircons: Ion microprobe evidence for high $\delta^{18}O$ continental crust and oceans in the Early Archean. Geochim. Cosmochim. Acta 65, 4215–4229.

Pickles, C.S., Kelley, S.P., Reddy, S.M., Wheeler, J., 1997. Determination of high spatial resolution argon isotope variations in metamorphic biotites. Geochim. Cosmochim. Acta 61, 3809–3883.

Pidgeon, R.T., Hallberg, J.A., 2000. Age relationships in supracrustal sequences of the northern part of the Murchison Terrane, Archaean Yilgarn Craton, Western Australia: a combined field and zircon U–Pb study. Aust. J. Earth Sci. 47, 153–165.

Pidgeon, R.T., Wilde, S.A., 1990. The distribution of 3.0 Ga and 2. 7 Ga volcanic episodes in the Yilgarn Craton of Western Australia. Precamb. Res. 48, 309–325.

Pidgeon, R.T., Wilde, S.A., 1998. The interpretation of complex zircon U–Pb systems in Archaean granitoids and gneisses from the Jack Hills, Narryer Gneiss Terrane, Western Australia. Precamb. Res. 91, 309–332.

Pidgeon, R.T., Furfaro, D., Clifford, B.A., 1994. Investigation of the age and rate of deposition of part of the Gossan Hill Group, Golden Grove using conventional single grain zircon U–Pb geochronology. Geol. Soc. Aust. Abstr. 37, 346.

Reddy, S.M., Potts, G.J., 1999. Constraining absolute deformation ages: the relationship between deformation mechanisms and isotope systematics. J. Struct. Geol. 21, 1255–1265.

Reddy, S.M., Kelley, S.P., Magennis, L., 1997. A microstructural and argon laser-probe study of shear zone development at the western margin of the Nanga Parbat – Haramosh Massif, western Himalaya. Contrib. Mineral. Petrol. 128, 16–29.

Rex, D.C., Guise, P.G., 1995. Evaluation of argon standards with special emphasis on time scale measurements. In: Odin, G.S. (Ed.), Phanerozoic Time Scale, vol. 13. Bull. Liais. Inform. IUGS Subcommission on Geochronology, pp. 21–23.

Rex, D.C., Guise, P.G., Wartho, J.-A., 1993. Disturbed ^{40}Ar-^{39}Ar spectra from hornblendes: thermal loss or contamination? Chem. Geol. (Isotope Geosci. Sect.) 103, 271–281.

Roddick, J.C., 1978. The application of isochron diagrams in $^{40}Ar/^{39}Ar$ dating: a discussion. Earth Planet. Sci. Lett. 41, 233–244.

Schiøtte, L., Campbell, I.H., 1996. Chronology of the Mount Magnet granite-greenstone terrain, Yilgarn Craton, Western Australia: implications for field based predictions of the relative timing of granitoid emplacement. Precamb. Res. 78, 237–260.

Sheppard, S., 2005. Does the ca. 1800 Ma Capricorn Orogeny mark collision of the Yilgarn and Pilbara Cratons? In: Wingate, M.T.D., Pisarevsky, S.A. (Eds.), Supercontinents and Earth Evolution Symposium. Geological Society of Australia Abstracts 81, p. 29.

Sheppard, S., Occhipinti, S.A., Tyler, I.M., 2003. The relationship between tectonism and composition of granitoid magmas, Yarlarweelor Gneiss Complex, Western Australia. Lithos 66, 133–154.

Sheppard, S., Occhipinti, S.A., Tyler, I.M., 2004. A 2005–1970 Ma Andean-type batholith in the southern Gascoyne Complex, Western Australia. Precamb. Res. 128, 257–277.

Sheppard, S., Occhipinti, S.A., Nelson, D.R., 2005. Intracontinental reworking in the Capricorn Orogen, Western Australia: the 1680–1620 Mangaroon Orogeny. Aust. J. Earth Sci. 52, 443–460.

Smith, P.E., York, D., Easton, R.M., Özdemir, Ö., Layer, P.W., 1994. A laser $^{40}Ar/^{39}Ar$ study of minerals across the Grenville Front: investigations of reproducible excess Ar patterns. Can. J. Earth Sci. 31, 808–817.

Spaggiari, C.V., 2006. Interpreted bedrock geology of the northern Murchison Domain, Youanmi Terrane, Yilgarn Craton. Western Australia. Geological Survey of Western Australia Record 2006/10.

Spaggiari, C.V., 2007a. Structural and lithological evolution of the Jack Hills greenstone belt, Narryer Terrane, Yilgarn craton: Western Australia Geological Survey, Record 2007/3.

Spaggiari, C.V., 2007b. The Jack Hills greenstone belt, Western Australia. Part 1. Structural and tectonic evolution over >1.5 Ga. Precamb. Res. 155, 204–228.

Spaggiari, C.V., Pidgeon, R.T., Wilde, S.A., 2007. The Jack Hills greenstone belt, Western Australia. Part 2. Lithological relationships and implications for the deposition of ≥4.0 Ga detrital zircons. Precamb. Res. 155, 261–286.

Steiger, R.J., Jäger, E., 1977. Subcommission on geochronology: convention on the use of decay constants in geo- and cosmochronology. Earth Planet. Sci. Lett. 36, 359–362.

Valley, J.W., Peck, W.H., King, E.M., Wilde, S.A., 2002. A cool early Earth. Geology 30, 351–354.

Vance, D., Ayres, M., Kelley, S.P., Harris, N.B.W., 1998. The thermal response of a metamorphic belt to extension: constraints from laser Ar data on metamorphic micas. Earth Planet. Sci. Lett. 162, 153–164.

Wang, Q., Schiøtte, L., Campbell, I.H., 1998. Geochronology of supracrustal rocks from the Golden Grove area, Murchison Province, Yilgarn Craton, Western Australia. Aust. J. Earth Sci. 45, 571–577.

Wartho, J.-A., Dodson, M.H., Rex, D.C., Guise, P.G., 1991. Mechanisms of argon release from Himalayan metamorphic hornblende. Am. Mineralogist 76, 1446–1448.

Wartho, J.-A., Rex, D.C., Guise, P.G., 1996. Excess argon in amphiboles linked to greenschist facies alteration in the Kamila Amphibolite Belt, Kohistan island arc system, northern Pakistan: Insights from $^{40}Ar/^{39}Ar$ step-heating and acid leaching experiments. Geol. Mag. 133, 595–609.

Watkins, K.P., Hickman, A.H., 1990. Geological evolution and mineralization of the Murchison Province, Western Australia. West. Aust. Geol. Surv. Bull. 137, 267.

Wilde, S.A., Pidgeon, R.T., 1990. Geology of the Jack Hills metasedimentary rocks. In: Ho, S.E., Glover, J.E., Myers, J.S., Muhling, J.R. (Eds.), Third International Archaean Symposium, Perth, Excursion Guidebook. Geology Department, University Extension. University of Western Australia Publication 21. University of Western Australia, Western Australia, pp. 82–95.

Wilde, S.A., Valley, J.W., Peck, W.H., Graham, C.M., 2001. Evidence from detrital zircons for the existence of continental crust and oceans on the Earth 4.4 Gyr ago. Nature 409, 175–178.

Williams, S.J., 1986. Geology of the Gascoyne Province Western Australia. Western Australia Geological Survey Report 15, 85 pp.

Williams, I.R., Myers, J.S., 1987. Archaean geology of the Mount Narryer region Western Australia: Western Australia Geological Survey, Report 22, 32 pp.

Williams, I.R., Walker, I.M., Hocking, R.M., Williams, S.J., 1983a. Byro, W.A., first ed. Western Australia Geological Survey, 1:250 000 Geological Series Explanatory Notes, 27 pp.

Williams, S.J., Williams, I.R., Hocking, R.M., 1983b. Glenburgh, W.A. Western Australia Geological Survey, 1:250,000 Geological Explanatory Notes, 25 pp.

Wingate, M.T.D., Morris, P.A., Pirajno, F., Pidgeon, R.T., 2005. Two large igneous provinces in Late Mesoproterozoic Australia. In: Wingate, M.T.D., Pisarevsky, S.A. (Eds.), Supercontinents and Earth Evolution Symposium. Geological Society of Australia Inc. Abstracts 81, p. 151.

Wyche, S., Nelson, D.R., Riganti, A., 2004. 4350–3130 Ma detrital zircons in the Southern Cross Granite-Greenstone Terrane, Western Australia: implications for the early evolution of the Yilgarn Craton. Aust. J. Earth Sci. 51, 31–45.